The Astrophysical Journal, 909:142 (23pp), 2021 March 10 https://doi.org/10.3847/1538-4357/abde37

The Source Locations of Major Flares and CMEs in Emerging Active Regions

Lijuan Liu[1,2,3], Yuming Wang[2,3], Zhenjun Zhou[1,3], and Jun Cui[1,4]
[1] Planetary Environmental and Astrobiological Research Laboratory (PEARL), School of Atmospheric Sciences, Sun Yat-sen University, Zhuhai, Guangdong 519082, People's Republic of China; liulj8@mail.sysu.edu.cn
[2] CAS Key Laboratory of Geospace Environment, Department of Geophysics and Planetary Sciences, University of Science and Technology of China, Hefei, Anhui 230026, People's Republic of China
[3] CAS center for Excellence in Comparative Planetology, People's Republic of China
[4] CAS Key Laboratory of Lunar and Deep Space Exploration, National Astronomical Observatories, Chinese Academy of Sciences, Beijing 100012, People's Republic of China
Received 2020 January 14; revised 2020 December 21; accepted 2021 January 18; published 2021 March 12

Abstract

Major flares and coronal mass ejections (CMEs) tend to originate from compact polarity inversion lines (PILs) in solar active regions (ARs). Recently, a scenario named "collisional shearing" was proposed by Chintzoglou et al. to explain the phenomenon, which suggests that the collision between different emerging bipoles is able to form a compact PIL, driving the shearing and flux cancellation that are responsible for the subsequent large activities. In this work, by tracking the evolution of 19 emerging ARs from their birth until they produce the first major flares or CMEs, we investigated the source PILs of the activities, i.e., the active PILs, to explore the generality of "collisional shearing." We find that none of the active PILs is the self PIL (sPIL) of a single bipole. We further find that 11 eruptions originate from the collisional PILs (cPILs) formed due to the collision between different bipoles, six from the conjoined systems of sPIL and cPIL, and two from the conjoined systems of sPIL and ePIL (external PIL between the AR and the nearby pre-existing polarities). Collision accompanied by shearing and flux cancellation is found to develop at all PILs prior to the eruptions, with 84% (16/19) cases having collisional length longer than 18 Mm. Moreover, we find that the magnitude of the flares is positively correlated with the collisional length of the active PILs, indicating that the more intense activities tend to originate from PILs with more severe collisions. The results suggest that "collisional shearing," i.e., bipole–bipole interaction during the flux emergence, is a common process in driving the major activities in emerging ARs.

Unified Astronomy Thesaurus concepts: Solar active regions (1974); Solar active region magnetic fields (1975); Solar activity (1475); Solar flares (1496); Solar coronal mass ejections (310)

Supporting material: animations

1. Introduction

Solar flares and coronal mass ejections (CMEs) are among the most violent activities in the solar atmosphere. Their main producers are known to be solar active regions (ARs). It is generally accepted that ARs are formed by magnetic flux emerging from the solar interior. The emergence of a single Ω-shaped flux tube can form the simplest bipolar region, the two polarities of which are the intersections between the axial field of the tube and the photosphere (Schmieder et al. 2014, and reference therein). During the emergence, the two main polarities move apart, with typical signatures such as small moving dipoles (small polarity pairs of opposite sign) appearing between them (e.g., Strous & Zwaan 1999; Bernasconi et al. 2002; Centeno 2012). Different bipoles can interact to form a complex configuration, such as a quadrupolar configuration.

Observationally, not all ARs are able to generate large flares or CMEs. It is found that the eruption-producing ARs tend to be larger, containing a larger amount of magnetic free energy and hosting a more complex configuration than a single bipole (e.g., Falconer et al. 2002, 2006, 2008; Leka et al. 2003; Georgoulis & Rust 2007; Leka & Barnes 2007; Chen et al. 2011; Liu et al. 2016). Enough free energy is only a necessary condition for the AR to produce major flares or CMEs. The trigger of the activities may involve more complex processes such as magnetohydrodynamics (MHD) instabilities (e.g., Török et al. 2004; Kliem & Török 2006) and magnetic reconnection (e.g., Antiochos et al. 1999; Moore et al. 2001). Considering the evolution of the ARs, their ability to produce eruptions increases as the flux emerges (van Driel-Gesztelyi & Green 2015, and reference therein). Although decaying ARs can also produce eruptions mainly due to flux cancellation (magnetic reconnection near the photosphere), the most violent activities tend to originate from ARs that are still emerging and evolving (Schrijver 2009).

The lines where the polarities change signs are called polarity inversion lines (PILs). It is found that within the eruption-producing ARs, compact PILs, i.e., PILs with a high spatial gradient, are usually the sources of major flares and CMEs (Schrijver 2007). Shearing motions and sunspot rotations can always be found near the compact PILs. Those motions are suggested to be able to shear or twist the field lines so as to inject free energy and magnetic helicity into the AR (e.g., Fan 2009; Yan et al. 2015), and thus are closely related to eruptions. Converging motions and flux cancellation are also frequently observed (e.g., Green et al. 2011; Cheng et al. 2014). In the classical flux cancellation model of the single bipolar region (van Ballegooijen & Martens 1989), converging motions can bring together footpoints of opposite sign from different loops of the sheared arcade, leading to flux cancellation, which forms the flux rope (a set of helical field lines winding around a common axis). The subsequent eruption of the flux rope may form the CME, and generate the flare through magnetic reconnection (e.g., Shibata et al. 1995).

Combining the shearing motion, converging motion, and flux cancellation in the emerging ARs, Chintzoglou et al. (2019) proposed a new scenario to explain the formation of compact PILs and the origin of the major solar activities. By tracking the evolution of two flare- and CME-productive ARs from the very beginning of their emergence, the authors found that clusters of eruptions correlated well with the onset of a process named "collisional shearing." During "collisional shearing," different bipoles appear on the photosphere due to the emergence of different flux tubes. For each bipole, the two main polarities move apart as the two legs of the flux tube separate during the emergence. The separation results in converging motions, and thus collision, between the nonconjugated polarities of opposite sign, forming the compact PIL. The continuous collision further drives shearing and flux cancellation, leading to magnetic reconnection and the formation of flux ropes, followed by a series of large activities. This kind of compact PIL formed by collision between nonconjugated polarities is defined as collisional PIL (cPIL), differentiating it from the self PIL (sPIL) formed between conjugated polarities (all defined in Chintzoglou et al. 2019). The authors pointed out that the overall PIL in an AR was naturally an integral system of sPIL and cPIL. They further identified two types of collisional shearing patterns, case A and case B. In case A, the two bipoles emerge simultaneously, driving the collision by self-separation. In case B, the two bipoles emerge sequentially, followed by the collision. In contrast to the eruption models considering bipolar ARs (e.g., van Ballegooijen & Martens 1989; Fan 2001), the bipole–bipole interaction plays the major role in the collisional shearing scenario.

Liu et al. (2019) also reported that during the early emergence phase of NOAA AR 12673, a magnetic flux rope above the AR's central PIL was formed through flux cancellation and shearing during the "collisional shearing." They further suggested that the subsequent recurrent eruptions and re-formation of flux ropes were driven by the same process. Both Chintzoglou et al. (2019) and Liu et al. (2019) indicate that the "collisional shearing" may be important in driving large solar activities in emerging ARs. However, no statistical study on this phenomenon has been done to the best of our knowledge. In this work, we perform statistical research on the evolution of 19 ARs from their birth until they produce their first major activity, i.e., a large flare ($\geqslant$M1.0 class) or a CME, to explore the generality of "collisional shearing." We mainly focus on the properties of the source PILs of those activities, which are named active PILs in the following.

The paper is organized as follows. In Section 2, we describe the event sample, the data, and the method we use. The statistical result and typical examples are presented in Section 3. We give the discussions and conclusions in Section 4.

2. Observation and Data Analysis

The 19 ARs we studied are selected from the list presented in Kutsenko et al. (2019), which contains 423 emerging ARs observed by the Helioseismic and Magnetic Imager (HMI; Scherrer et al. 2012) on board Solar Dynamics Observatory (SDO; Pesnell et al. 2012). Our ARs fulfill the following criteria: the AR should emerge and generate at least one major flare ($\geqslant$M1.0 class, either confined or not) or CME within the region between Stonyhurst longitudes 60°E and 60°W (roughly having disk-centered angle $\Theta \leqslant 60°$). The criteria ensure a relatively high signal-to-noise ratio of the HMI data, because the data taken near the solar limb are subjected to severe uncertainties and the projection effect. We check the flares in the soft X-ray (SXR) flare catalog of the Geostationary Operational Environmental Satellite (GOES).[5] The CMEs are examined in the Solar and Heliospheric Observatory (SOHO)/Large Angle and Spectrometric Coronagraph (LASCO) CME catalog maintained at the Coordinated Data Analysis Workshop (CDAW) data center[6] (Gopalswamy et al. 2009), and the Solar Terrestrial Relations Observatory (STEREO)/Sun–Earth Connection Coronal and Heliospheric Investigation (SECCHI) COR2 CME catalog that is recorded by the Solar Eruptive Event Detection System (SEEDS) maintained by the George Mason University[7] (Olmedo et al. 2008). The basic properties of the ARs and their first major activities are given in Table 1.

We use a data product from the SDO/HMI called Space-weather HMI Active Region Patches (SHARPs; Bobra et al. 2014; Hoeksema et al. 2014) to track the evolution of the ARs. The SHARP data series produces cutout maps of the automatically tracked ARs for their entire transit, providing the photospheric vector magnetic field as well as the line-of-sight (LOS) magnetograms with a spatial resolution of 0.″5 and a time cadence of 12 minutes. A specific version of the SHARP data, which is remapped from the CCD coordinates to the heliographic cylindrical equal-area (CEA) projection coordinates, is used. To locate the exact source PILs of the first major activities, we inspect the extreme ultraviolet (EUV) and ultraviolet (UV) images provided by the Atmospheric Imaging Assembly (AIA; Lemen et al. 2012) on board SDO. The images have a spatial resolution of 0.″6 and a time cadence up to 12 s. We mainly use the hot passband 131 Å ($\sim$10 MK) and the cool passband 304 Å ($\sim$50,000 K) to show the eruption details. If the eruption signatures are not clear enough in the two passbands, the 211 Å passband ($\sim$2.0 MK) is further used to show the possible coronal dimmings associated with the CMEs.

We follow the methods employed in Chintzoglou et al. (2019) to quantify the "collisional shearing" process. Specifically, we calculate the magnetic flux of the AR, track all polarities involved, and identify the collisional portions of the active PILs using the SHARP data. The radial component of the vector field, B_r, is a natural choice to do the analysis. However, the noise level of the vector field is as high as 100 G (Hoeksema et al. 2014), and is severe in the regions beyond 30° from the disk center. The other choice is to use the low-noise (as low as 10 G) radialized LOS magnetic field data, i.e., the LOS data corrected by dividing by the cosine of the angle between LOS and local normal of the disk ($B_{\rm los} = B_{\rm los}^{\rm raw} / \cos\theta$, in which $B_{\rm los}^{\rm raw}$ is the raw LOS data). In the following, the mentioned $B_{\rm los}$ indicates the data after correction. Nevertheless, the correction assumes that the horizontal component of the magnetic field (B_h) contributes much less to $B_{\rm los}$ than the vertical component (B_r), which may

[5] https://www.ngdc.noaa.gov/stp/space-weather/solar-data/solar-features/solar-flares/x-rays/goes/xrs/

[6] https://cdaw.gsfc.nasa.gov/CME_list/

[7] http://spaceweather.gmu.edu/seeds/secchi.php

Table 1
Information on the ARs, Their First Major Activities, and the Active PILs

No.	ARs			First Major Activities				Active PIL			
	NOAA No.	Flux Emergence Onset[a]		Flare[b]			CME Speed[c] (km s^{-1})	Collisional Shearing Case[d]	PIL Type[e]	$\overline{L}_{\rm cPIL}$[f]	$\overline{S}$[g]
		Time	Location	Start	Location	Class					
1	11081	2010-06-11T02:24	N24W32 (43°)	2010-06-12T00:30	N23W43 (52°)	M2.0	486	B	S/C	49.5 ± 12.8	61.7 ± 6.9
2	11158	2011-02-10T17:48	S20E47 (48°)	2011-02-13T17:28	S19W03 (15°)	M6.6	373	A	C	62.7 ± 3.8	70.1 ± 1.1
3	11162	2011-02-17T14:00	N18E15 (29°)	2011-02-18T10:23	N18E02 (26°)	M1.0		B	C	87.5 ± 6.4	77.9 ± 4.2
4	11422	2012-02-18T10:00	N16E25 (33°)	2012-02-19T08:41	N17E10 (26°)	C1.0	238	B	S/E	11.7 ± 2.2	48.6 ± 7.2
5	11440	2012-03-20T04:00	S26W00 (18°)	2012-03-21T12:38	S27W20 (25°)	C2.9	387	A	S/C	24.9 ± 6.5	61.2 ± 4.3
6	11466	2012-04-20T21:24	N13E58 (61°)	2012-04-27T08:15	N12W30 (35°)	M1.0	365	B	S/C	22.3 ± 6.4	67.6 ± 5.8
7	11620	2012-11-24T23:00	S13W02 (15°)	2012-11-27T21:05	S14W41 (43°)	M1.0		B	C	60.1 ± 4.5	59.9 ± 1.7
8	11675	2013-02-15T22:12	N12E47 (51°)	2013-02-17T15:45	N12E22 (30°)	M1.9		A	C	39.4 ± 7.4	61.7 ± 3.4
9	11762	2013-06-01T03:36	S29E04 (29°)	2013-06-03T07:03	S27W21 (38°)	C9.5	429[h]	B	S/C	61.0 ± 7.3	36.1 ± 2.1
10	11776	2013-06-18T07:12	N11E15 (18°)	2013-06-19T00:50	N10E03 (10°)	C2.3	287	A	S/C	20.0 ± 1.6	59.5 ± 5.9
11	11817	2013-08-10T09:36	S21E44 (51°)	2013-08-11T21:47	S20E25 (36°)	C8.4	110	A	C	69.1 ± 4.6	62.3 ± 2.0
12	11870	2013-10-13T05:00	S14E19 (28°)	2013-10-16T15:03	S15W29 (33°)	C1.8	514	B	S/E	4.3 ± 1.6	89.9 ± 15.9
13	11891	2013-11-05T12:48	S18E09 (25°)	2013-11-08T09:22	S17W28 (37°)	M2.3	207	A	C	41.8 ± 3.8	67.3 ± 2.4
14	11899	2013-11-15T15:24	N10E32 (47°)	2013-11-23T02:20	N14W56 (56°)	M1.1	406	A	C	61.7 ± 6.5	55.8 ± 3.4
15	11928	2013-12-16T08:24	S16E31 (35°)	2013-12-22T08:05	S19W51 (51°)	M1.9	231	A	C	70.9 ± 5.7	61.8 ± 1.6
16	11946	2014-01-04T05:12	N09E49 (51°)	2014-01-07T03:49	N07E08 (13°)	M1.0		B	C	19.5 ± 3.4	54.7 ± 2.4
17	12017	2014-03-23T22:36	N03E53 (54°)	2014-03-28T19:04	N11W21 (25°)	M2.0	420	B	C	44.3 ± 2.1	58.2 ± 2.9
18	12085	2014-06-05T22:36	S20E39 (44°)	2014-06-09T01:14	S20E00 (21°)	C3.7	417	B	S/C	30.3 ± 5.8	62.9 ± 3.9
19	12089	2014-06-10T20:00	N18E32 (35°)	2014-06-10T23:46	N17E29 (34°)	C2.1	343	A	C	12.9 ± 7.4	56.6 ± 10.6

Notes.
[a] The onset time and location of the flux emergence of the ARs. The locations are the Stonyhurst coordinates (outside the brackets) and the disk-centered angles (in the brackets). The time and Stonyhurst locations are cited from Kutsenko et al. (2019).
[b] The onset time, location (Stonyhurst and disk-centered angles), and class of the flares, referred to the GOES flare catalog (see Footnote 5).
[c] CME velocities provided by the SOHO/LASCO CME catalog. A blank in this column means no CME is associated with the flare.
[d] Collisional shearing case of the two colliding bipoles. Case A and case B stand for simultaneous and sequential collisional shearing, respectively.
[e] Type of the PILs. Here we use "C," "S/C," and "S/E" to represent the cPIL, conjoined sPIL/cPIL, and conjoined sPIL/ePIL for convenience.
[f] $\overline{L}_{\rm cpil}$: Length of the collisional parts of the PILs averaged over three hours prior to the activities. The standard deviations are taken as the errors. The collisional parts of the PILs are detected at the threshold of 100 G on the B_r data set.
[g] $\overline{S}$: Shear angles of the field at the collisional parts of the PILs, which are averaged over three hours prior to the activities. The standard deviations are taken as the errors.
[h] CME velocity provided by the STEREO/SECCHI COR2 CME catalog.

not hold when the AR is not near the disk center. The uncertainty introduced by the correction is hard to estimate without a low-noise B_h. Overall, the two data sets (B_r and $B_{\rm los}$) are safe to use in the region having disk-centered angle $\leqslant 30°$, but have different flaws outside the region. We thus repeat the analysis on both data sets for comparison.

The flux-weighted centroid for each polarity is calculated within a radius of 5 Mm (about 14 pixels) around its peak intensity (used in Chintzoglou et al. 2019). Note that some like-signed polarities from different bipoles may be extremely close to each other, having inseparable boundaries, and thus are called a group (defined in Chintzoglou et al. 2019). Based on the time-series centroids, we plot the trajectory of each centroid and the evolution of distances between different centroids.

We further quantify the collision strength and the non-potential shear of the active PILs. The collision strength is characterized by the length of the collisional, i.e., the compact part of the PIL with a high spatial gradient that is obtained by the method described in Schrijver (2007) and Chintzoglou et al. (2019). For the polarities forming the active PIL, the strong-field regions (kernels) are first isolated with various thresholds, then dilated by a kernel with a size of 5 pixels (the size used in Chintzoglou et al. 2019). The region where the positive and negative polarities intersect is taken as the primary collisional PIL part, as in Chintzoglou et al. (2019). A thinning operation is further performed until the part is 1 pixel wide (see details in Chintzoglou et al. 2019), which is taken as the final collisional PIL part. All pixels of the collisional part are summed up to get its length, $L_{\rm cPIL}$. Here various thresholds are used to avoid bias, which are 100, 125, 150, and 175 G for B_r, and 50, 75, 100, 125, 150, and 175 G for $B_{\rm los}$. As the collision is detected through the dilation of a strong-field kernel, a threshold lower than 50 G may not fit the definition of strong field, and one larger than 175 G may unnecessarily reduce the collisional length. The reason for not using 50 and 75 G for B_r is that they are lower than the noise level of B_r. It is found that all thresholds yield similar results (see Section 3.4). We thus present the results of B_r at 100 G (threshold used in Chintzoglou et al. 2019) for simplicity when showing the examples.

The non-potential shear is characterized by the mean shear angle S of the field in the collisional PIL part. To calculate the mean shear angle, we first compute the potential field with the Fourier transformation method (Alissandrakis 1981) using photospheric B_r as the input, then calculate the mean shear angle S from the equation $S = \frac{1}{N}\Sigma\arccos\left(\frac{\boldsymbol{B}^{\rm Obs}\cdot\boldsymbol{B}^{\rm pot}}{|\boldsymbol{B}^{\rm Obs}||\boldsymbol{B}^{\rm Pot}|}\right)$ (Bobra et al. 2014), in which N is the number of pixels of the collisional part of the PIL, $\boldsymbol{B}^{\rm Obs}$ is the observed vector magnetic field, and $\boldsymbol{B}^{\rm pot}$ is the extrapolated potential field. For the LOS field data set, S is calculated in the same way using the collisional pixels identified on $B_{\rm los}$ maps.

We further inspect the difference between the parameters obtained on B_r and $B_{\rm los}$ data sets. For two values calculated on different data sets at the same time, their percentage difference is measured as $r = \frac{p_{\rm los} - p_r}{p_r} \times 100\%$, in which $p_{\rm los}$ and p_r indicate $L_{\rm cPIL}$ or S obtained on $B_{\rm los}$ and B_r, respective. The overall difference is then calculated as the mean value of the percentage differences of all data, $\frac{1}{N}\Sigma r$, in which N is the number of data points from the start of flux emergence to the flare onset.

3. Results

We track the ARs and locate the active PILs where the first major activities originate. For an AR, apart from the sPIL and cPIL (defined in Chintzoglou et al. 2019), there may be another type of PIL formed between the AR and the nearby pre-existing polarities, defined as the external PIL (ePIL, Mackay et al. 2008; Chintzoglou et al. 2019). We find that the active PILs in our sample could be classified into three types: cPIL, of which the PILs are complete collisional PILs; conjoined sPIL/cPIL, in which the PILs are a combination of self PILs and collisional PILs; and conjoined sPIL/ePIL, in which the PILs are integral systems of self PILs and external PILs. Finally, we get 11 cPILs, six conjoined sPIL/cPIL, and two conjoined sPIL/ePIL. Their information is shown in Table 1. Eight typical examples are given in the following.

3.1. Examples of cPILs

3.1.1. The cPIL in NOAA AR 11162

NOAA AR 11162 is composed of two bipoles emerging sequentially. Its collisional shearing is of case B. From the start of flux emergence to the flare onset, the AR transits from Stonyhurst longitude 10°E to 0°E, with its disk-centered angle changing from 28°.1 to 26°.3. The evolution of the AR is shown in Figure 1, which displays the B_r magnetograms, the centroids of polarities and their distances obtained on B_r, and the length and shear angle of the collisional PIL parts detected at 100 G on both B_r and $B_{\rm los}$ data sets. We determine the conjugated polarities of a bipole according to three criteria: first, the two polarities emerge at the same time; second, they move apart from each other; third, typical signatures such as moving dipoles appear between them.

The first bipole, named bipole A, starts to emerge at around 2011 February 17T15:34. Four hours later, the other bipole, bipole B, emerges to the west of bipole A, with its positive polarity (PB in Figure 1) located close to the negative polarity of bipole A (NA in Figure 1). As emergence proceeds, the conjugated polarities of each bipole separate, causing the nonconjugated NA and PB to approach each other. The PIL between NA and PB is the active PIL (cyan line in Figure 1). On the PIL, a collisional signature appears and grows gradually (red line part in Figure 1). A clear disappearance of the negative polarities is observed near the PIL (enclosed in magenta circle in Figure 1), indicating flux cancellation. We further track the motion of the flux-weighted centroids of all polarities and show their trajectories in Figure 1(g). The centroid of NA moves northwestward, while that of PA first moves southwestward then northeastward. Meanwhile, the centroid of NB moves westward, while that of PB moves eastward. NA and PB slightly approach and shear against each other. Since the active PIL is formed by the collision of nonconjugated polarities, we classify it as a cPIL.

The evolution of the distances between the polarities further proves the "separation and collision" process (Figure 1(h)). From the start of flux emergence to the flare onset, both the distances between the conjugated polarities of bipole A and bipole B increase. The former increases from 19.8 to 31.1 Mm, while the latter grows from 18.7 to 31.0 Mm. The distance between NA and PB slightly decreases from 20.5 to 18.3 Mm. When the first major activity occurs, the AR grows into a medium sized region with unsigned magnetic flux of 8.0×10^{21} Mx (Figure 1(i)). The length of the collisional PIL

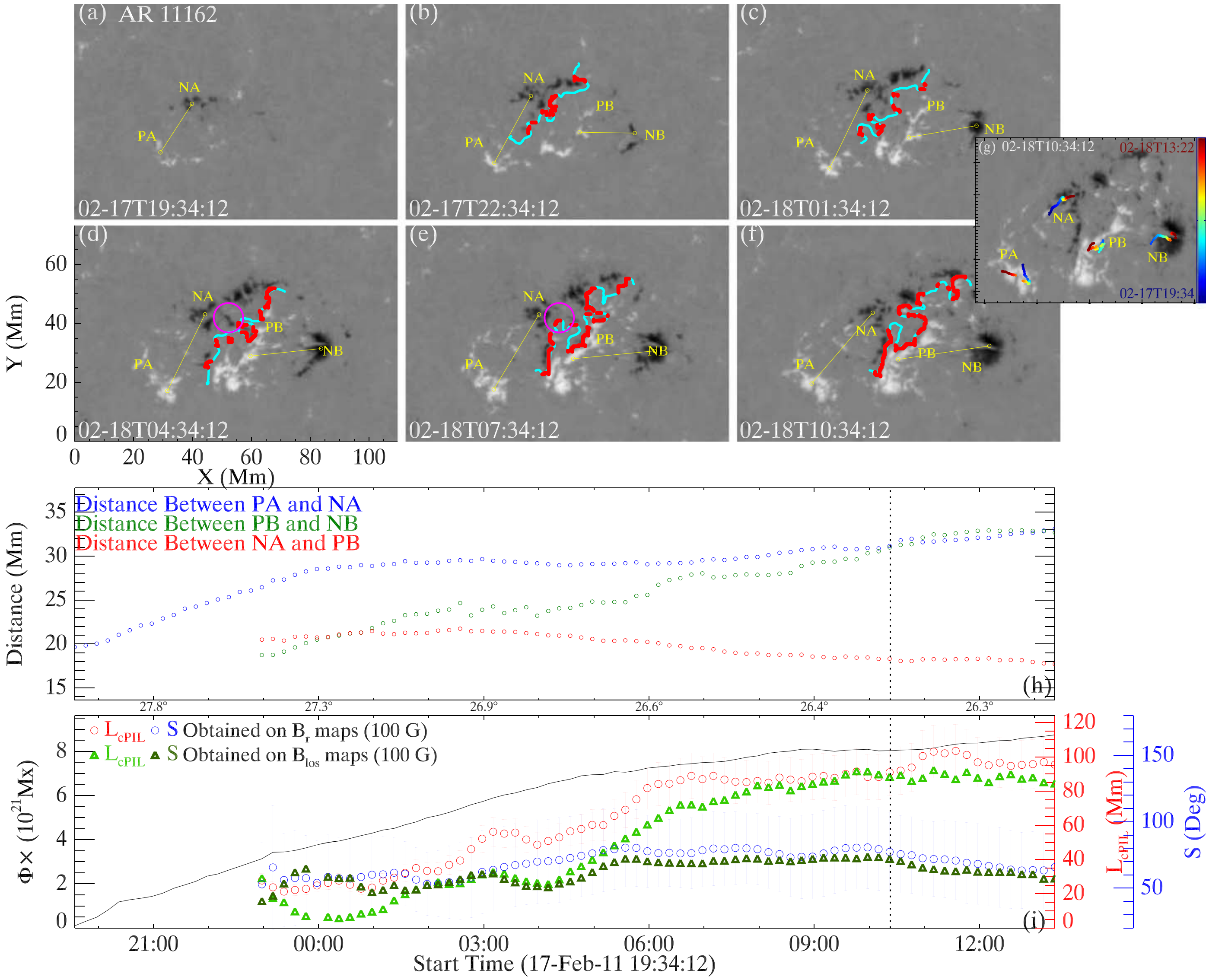

Figure 1. Evolution of NOAA AR 11162. (a)–(f) Evolution of the photospheric B_r. White (black) patches are the positive (negative) polarities, saturating at ±2000 G. PA and NA indicate the positive and negative polarities of bipole A, while PB and NB are for bipole B. The cyan lines mark the source PIL of the first major activity; they are obtained from the contours at $B_r = 0$. The red lines indicate the collisional components of the PILs. The collisional parts are obtained by the method described in Section 2. The yellow circles mark the flux-weighted centroids of the polarities, with those of the conjugated polarities connected by yellow lines. The magenta circles in panels (d) and (e) mark the location where a patch of negative polarity disappears. An animation of the magnetograms lasting from 2011 February 17T14:10 to 2011 February 18T12:58 is available online. (g) The trajectories of the flux-weighted centroids of all polarities tracked on the B_r data set. As time elapses, the color of the dots changes from blue to red. (h) Evolution of the distances between each pair of conjugated polarities and between the colliding, nonconjugated polarities. (i) Evolution of the magnetic flux (Φ), the length ($L_{\rm cPIL}$), and mean shear angle (S) of the collisional part of the PIL obtained on both B_r and radialized $B_{\rm los}$ data sets at the threshold of 100 G. Errors for the $L_{\rm cPIL}$ from B_r are further shown, accounting for 15% of the values of $L_{\rm cPIL}$. The percentage is estimated by Chintzoglou et al. (2019) using the same cPIL detection method. The errors for S are the standard deviations of the shear angles of the collisional parts of the PILs. Vertical lines in (h) and (i) mark the moment of onset of the flare. The locations at the top of panel (i) are disk-centered angles of the AR at the relevant timings.

(An animation of this figure is available.)

part ($L_{\rm cPIL}$) obtained on the B_r series has increased from 27.8 to 91.0 Mm, while the mean shear angle (S) increases from 64°.1 to 77°.3. $L_{\rm cPIL}$ and S obtained on the $B_{\rm los}$ series show a similar trend. The former increases from 18.5 to 88.3 Mm, and the latter from 54°.4 to 72°.2. The overall difference between $L_{\rm cPIL}$ on the two data sets is −24.5%, and that for S is −10.0%, indicating that both parameters obtained on $B_{\rm los}$ are overall smaller than those obtained on B_r at the same threshold in this event.

The first major eruption from the AR is an M1.0 class flare accompanied by the failed eruption of a filament that launches at 2011 February 18T10:23 (Figure 2). In both the hot and cool AIA channels, 131 Å and 304 Å passbands, the eruption of the filament is observed to occur above the cPIL between NA and PB (blue lines in Figure 2). The brightenings at the PIL and the flaring ribbons occurring on both sides of the cPIL in the 1600 Å passband (black contours in Figure 2) confirm that the cPIL is the source of the eruption.

3.1.2. The cPIL in NOAA AR 11891

NOAA AR 11891 starts to emerge from around 2013 November 5T12:48. It transits from Stonyhurst longitude 09°E to 31°W until the first major activity, with the disk-centered

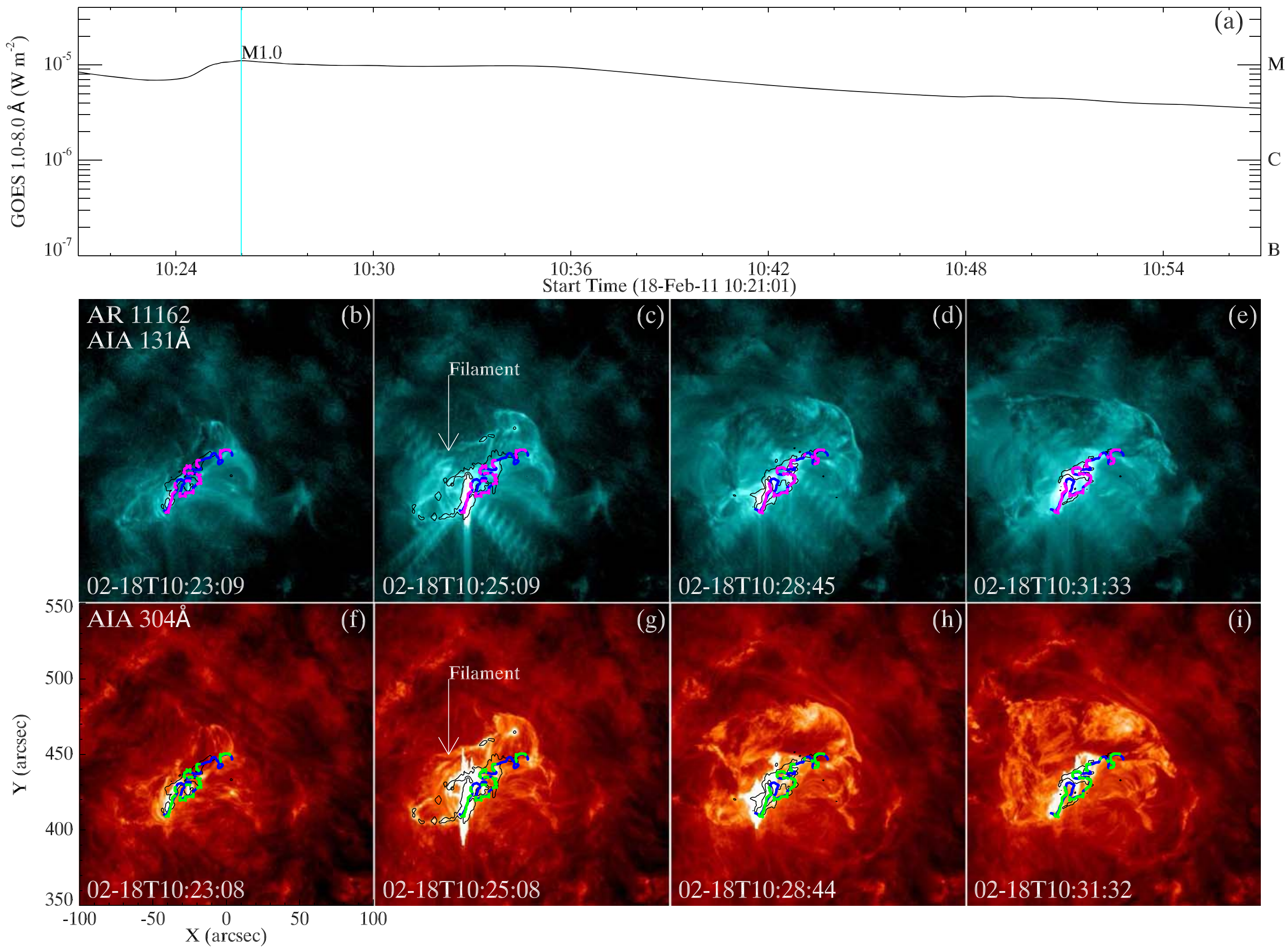

Figure 2. The first major activity occurred in NOAA AR 11162. (a) GOES 1–8 Å flux. The vertical line indicates the instant of the peak of the flare. (b)–(e) Eruption details captured in the AIA 131 Å passband. (f)–(i) Eruption details observed in the AIA 304 Å passband. Blue lines in (b)–(i) indicate the source PIL of the eruption, i.e., the PIL between NA and PB as shown in Figure 1. Purple lines in (b)–(e) and green lines in (f)–(i) mark the collisional part of the PIL. The black contours in panels (b)–(i) outline the flare ribbons in the 1600 Å passband. An associated animation lasting from 2011 February 18T10:23 to 2011 February 18T10:46 is available online.

(An animation of this figure is available.)

angle changing from 24°.5 to 36°.8. The evolution of the AR is shown in Figure 3. Two bipoles, named A and B, appear on the photosphere simultaneously. Its collisional shearing belongs to case A. The conjugated polarities of each bipole move apart from each other, while the positive polarity of bipole A (PA) and the negative polarity of bipole B (NB) approach each other (see Figures 3(a)–(f) and the associated movie). The PIL between the two nonconjugated polarities is the active PIL (cyan lines in Figures 3(a)–(f)). Collisional signatures gradually appear on the PIL (red line parts in Figures 3(a)–(f)). It is thus classified as a cPIL. During the collision, the conjugated polarities of the two bipoles keep separating, so that the nonconjugated polarities PA and NB shear against each other. Shrinkage of the negative polarities is observed near the PIL (enclosed in magenta circles in Figure 3), indicating flux cancellation. The trajectories of the flux-weighted centroids of the polarities confirm the above process (Figure 3(g)). PA moves northwestward while NA moves northeastward. PB moves westward while NB moves southeastward. The nonconjugated PA and NB first approach and then slide away from each other. The slight discontinuity of the trajectories results from the jump in the positions of the centroids.

Until the flare, the distance between PA and NA increases from 15.1 to 36.5 Mm, and that between PB and NB increases from 23.3 to 44.2 Mm, confirming the separation of the conjugated polarities (Figure 3(h)). The distance between PA and NB first decreases from 13.5 to 6.1 Mm, then increases to 16.0 Mm, consistent with their collision and shearing-away motion. The unsigned magnetic flux of the AR increases to 7.7×10^{21} Mx (Figure 3(i)). The length of the collisional PIL part obtained on the B_r series increases from 10.9 to 43.0 Mm and the mean shear angle increases from 60°.2 to 68°.1. $L_{\rm cPIL}$ obtained on $B_{\rm los}$ also increases from 12.8 to 52.0 Mm, while S slightly decreases from 60°.0 to 52°.8. The overall difference in $L_{\rm cPIL}$ from the two data sets is 25.3%, while that in S is -10.9%, indicating that in this case $L_{\rm cPIL}$ obtained from $B_{\rm los}$ is larger than the value obtained from B_r while S is smaller.

The first major eruption from this AR is an M2.3 class flare that starts from 2013 November 8T09:22. It is accompanied by a CME propagating away with a velocity of around 207 km s^{-1}

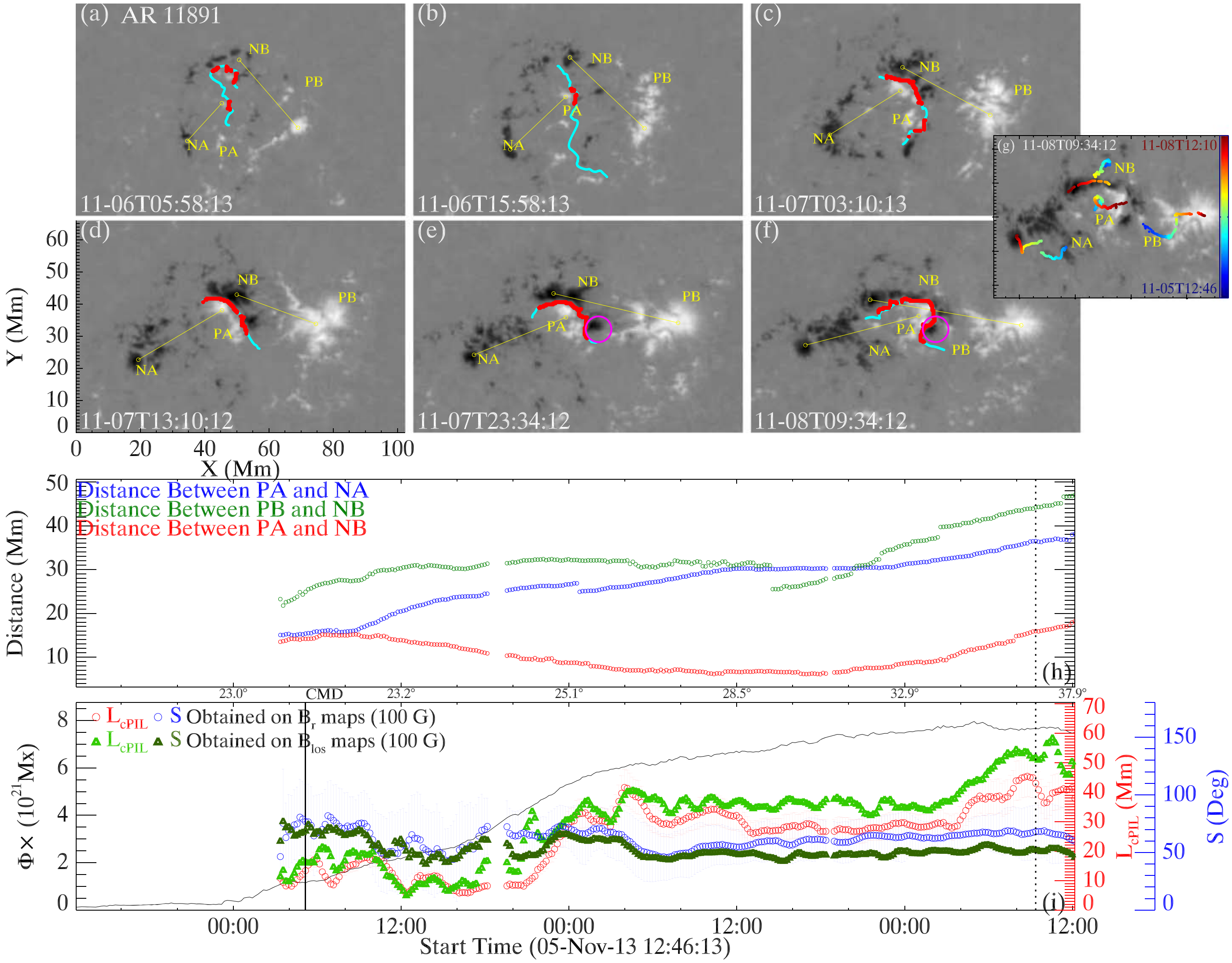

Figure 3. The evolution of NOAA AR 11891. Same layout as Figure 1. An animation of the magnetograms lasting from 2013 November 5T12:58 to 2013 November 8T12:10 is available online. The solid vertical line labeled as "CMD" marks the instant when the AR passes the central meridian.

(An animation of this figure is available.)

(see also Table 1). Brightenings at the cPIL between PA and NB are observed in both the 131 Å and 304 Å passbands, revealing that the eruption initiates here (Figure 4). Moreover, mass eruption is seen in the 304 Å passband (Figure 4(g)). Post-flare loops appear across the PIL in the 131 Å passband after the flare (Figure 4(e)). The flaring ribbons appear on both sides of the cPIL in the 1600 Å passband (black contours in Figure 4), confirming that the cPIL is the source of the eruption.

3.1.3. The cPIL in NOAA AR 12089

NOAA AR 12089 is composed of two bipoles, A and B, which start to emerge from around 2014 July 10T20:22 simultaneously. Its collisional shearing belongs to case A. Until the flare, the AR crosses the region between Stonyhurst longitudes 31°E and 28°E, with the disk-centered angle changing from 35°.2 to 33°.6. The nonconjugated polarities NA and PB stay quite close (Figures 5(a)–(f)), so that the PIL between them is classified as a cPIL. The first major activity occurs only 4 hr after the onset of emergence, thus the conjugated polarities do not separate too much as shown by the trajectories of their flux-weighted centroids (Figure 5(g)). The PA slightly moves to the northeast while NA moves northwestward. In the meantime, PB moves southward while NB moves westward. The distance between PA and NA slightly increases from 12.1 to 13.5 Mm, and that between PB and NB remains around 11.8 Mm (Figure 5(h)). NA and PB also have a separation remaining around 6.0 Mm, supporting the idea that the two polarities are quite close from their emergence. Until the flare, the AR is still small, having unsigned magnetic flux of 1.2×10^{21} Mx (Figure 5 (i)). The length of the cPIL between NA and PB (obtained on B_r) increases from 1.1 to 9.8 Mm, and the mean shear angle fluctuates slightly around 55°.0. For $L_{\rm cPIL}$ and S obtained on $B_{\rm los}$, the former increases from 1.5 to 12.9 Mm, and the latter also fluctuates slightly around 55°. The overall difference of the two sets of $L_{\rm cPIL}$ is −5.8%, while that of S is 4.1%, which are all relatively small.

The first major activity from the AR is a CME propagating with a velocity of around 343 km s^{-1}, accompanied by a C2.1 class flare that starts from 2014 July 10T23:46 (Figure 6). In the AIA 131 Å passband, brightenings are observed to occur at

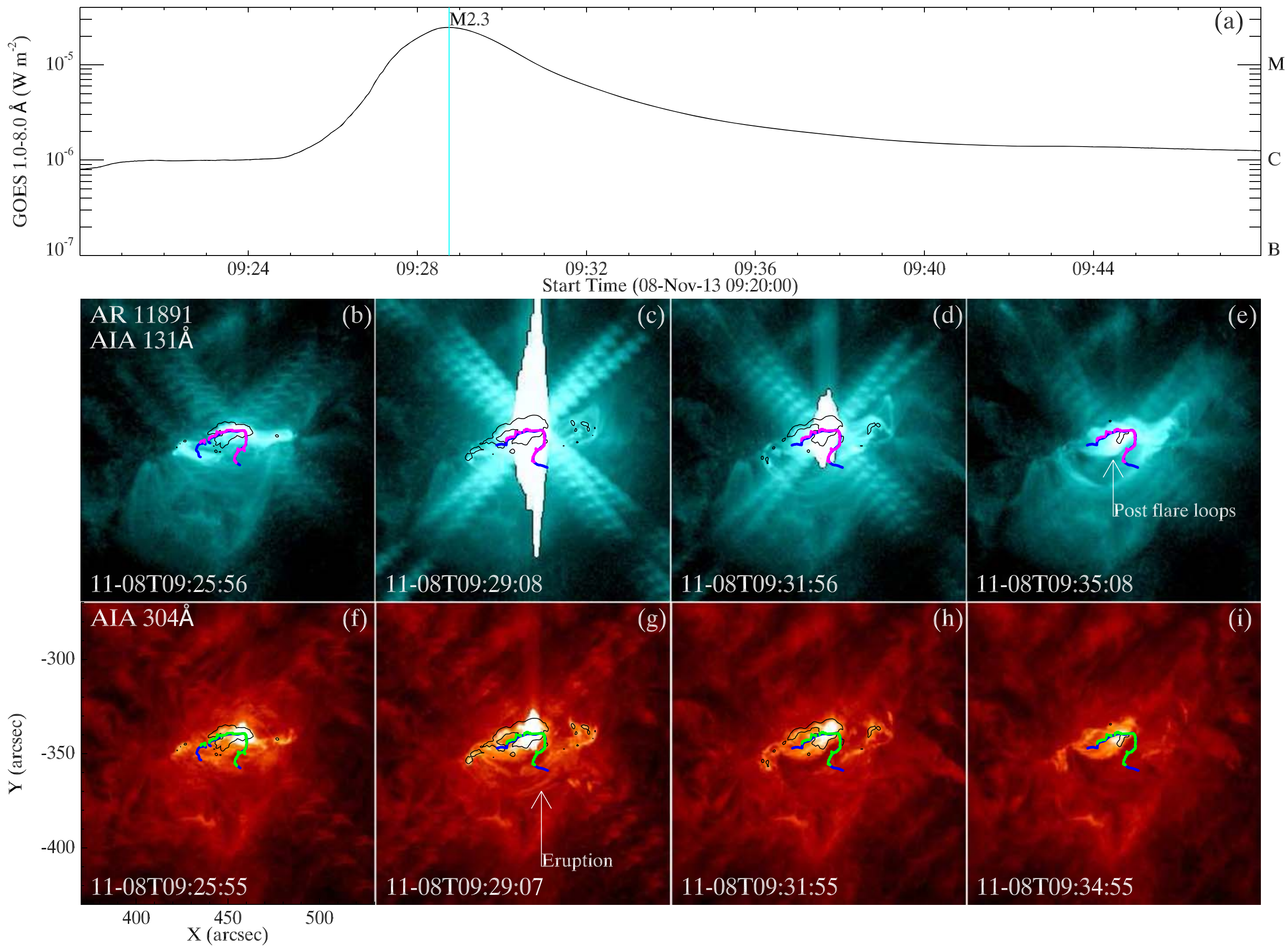

Figure 4. The first major activity that occurred in NOAA AR 11891. Same layout as Figure 2. An animation lasting from 2013 November 8T09:25 to 2013 November 8T09:37 is available online.

(An animation of this figure is available.)

the cPIL between NA and PB. Clear dimmings are observed near the cPIL in the AIA 211 Å passband, which indicates mass depletion during the CME. The flaring ribbons occurring along both sides of the cPIL in the 1600 Å passband confirm that it is the source PIL.

3.2. Examples of the Conjoined sPIL/cPIL

3.2.1. The Conjoined sPIL/cPIL in NOAA AR 11081

NOAA AR 11081 presents a multipolar configuration, which is composed of more than three bipoles emerging sequentially. We focus on the two lately emerged bipoles, which are named as bipole A and bipole B. From their emergence until the flare, the AR transits from Stonyhurst longitude 38°W to 49°W, with the disk-centered angle changing from 43°.4 to 51°.9. Bipole A starts to emerge from around 2010 July 11T06:22 (see Figures 7(a)–(f)). About 9 hr later, bipole B starts to emerge to the west of bipole A, with both its polarities (PB and NB) located close to the negative polarity of bipole A (NA). As emergence proceeds, NA gradually intrudes in between PB and NB. A PIL can be drawn between PB and the group of NB and NA (cyan line in Figure 7), which is the active PIL of the AR. Collisional signatures appear on it (red line parts in Figure 7). Shrinkage of the positive polarities is also observed (enclosed in magenta circles in Figure 7), indicating flux cancellation. Since the PIL is an integral system of the sPIL between PB and NB and the cPIL between PB and NA (first identified in Chintzoglou et al. 2019), it is classified as a conjoined sPIL/cPIL. The trajectories of the flux-weighted centroids show that PA moves northeastward while NA moves southwestward. PB first moves to the northwest then turns to the southwest, while NB moves southwestward (Figure 7(g)).

Until the flare, the distance between PA and NA increases from 25.4 to 52.4 Mm, and that between NB and PB increases from 13.4 to 24.0 Mm, supporting the separation of conjugated polarities (Figure 7(h)). The distance between NA and PB remains relatively invariant around 10 Mm, which indicates that the collision starts with the emergence of bipole B. The collisional shearing is thus case B. The unsigned magnetic flux of the AR grows to 8.5×10^{21} Mx (Figure 7(i)). The length of the collisional PIL part obtained on B_r increases from 25.1 to 70.8 Mm, and the mean shear angle slightly increases from 54°.9 to 62°.1. $L_{\rm cPIL}$ and S obtained on $B_{\rm los}$ show a similar trend. The former increases from 11.1 to 66.8 Mm, and the latter from 37°.6 to 52°.0. The difference in $L_{\rm cPIL}$ from the two data sets is

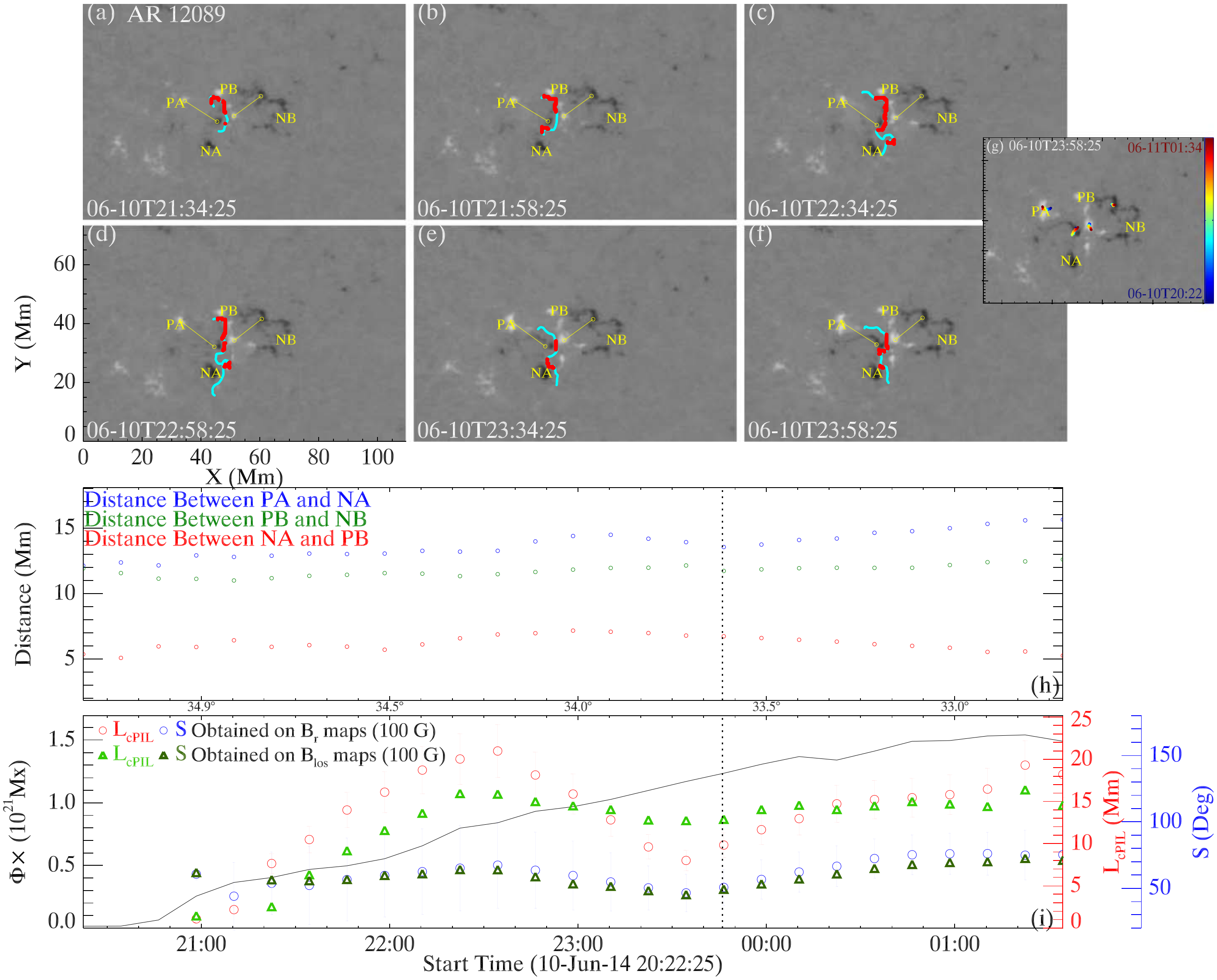

Figure 5. The evolution of NOAA AR 12089. Same layout as Figure 1. An animation of the magnetograms lasting from 2014 July 10T20:22 to 2014 July 12T22:46 is available online.

(An animation of this figure is available.)

-16.3%, and that in S is -27.1%, indicating that the values from $B_{\rm los}$ are smaller than those from B_r in this event.

The first major activity of the AR is an M2.0 class flare that starts from 2010 July 12T00:30, accompanied by a CME propagating away with a velocity of 486 km s^{-1} (Figure 8). In both the AIA 131 Å and 304 Å passbands, brightenings and mass eruption are observed near the active PIL. The flaring ribbons in the 1600 Å passband appear on both sides of the PIL, confirming it is the source of the eruption.

3.2.2. The Conjoined sPIL/cPIL in NOAA AR 11440

NOAA AR 11440 transits from Stonyhurst longitude 00°E to 19°W until the flare, with its disk-centered angle changing from 18°.1 to 24°.9. It exhibits a multipolar configuration, which can be roughly divided into three bipoles (Figures 9(a)–(f)). We focus on the two bipoles that emerge from around 2012 March 21T02:58, named bipoles A and B. They emerge simultaneously. The collisional shearing is case A. Bipole B is located to the west of bipole A, being closer to PA. As emergence proceeds, PA moves in between PB and NB, forming a PIL between NB and the group of PA and PB (cyan line in Figure 9). Collision signatures are observed on the PIL from the early stage of the emergence (red line part in Figure 9). Disappearance of small patches of polarities, which indicates flux cancellation, is observed at the PIL (see the movie associated with Figure 9). Since the PIL is an integral system of sPIL and cPIL, we classify it as a conjoined sPIL/cPIL. The trajectories of the flux-weighted centroids of the polarities show (Figure 9(g)) that PA moves westward while NA moves southeastward; PB moves northwestward while NB moves eastward.

Until the flare, the distance between PA and NA increases from 13.1 to 28.1 Mm (Figure 9(h)), and that between PB and NB from 16.2 to 27.1 Mm. The distance between PA and NB remains almost unchanged around 10 Mm. The results prove the separation between the conjugated polarities, and quite a close distance between PA and NB from the onset of emergence. The AR grows into a medium sized region with unsigned magnetic flux of 3.4×10^{21} Mx (Figure 9(i)). The

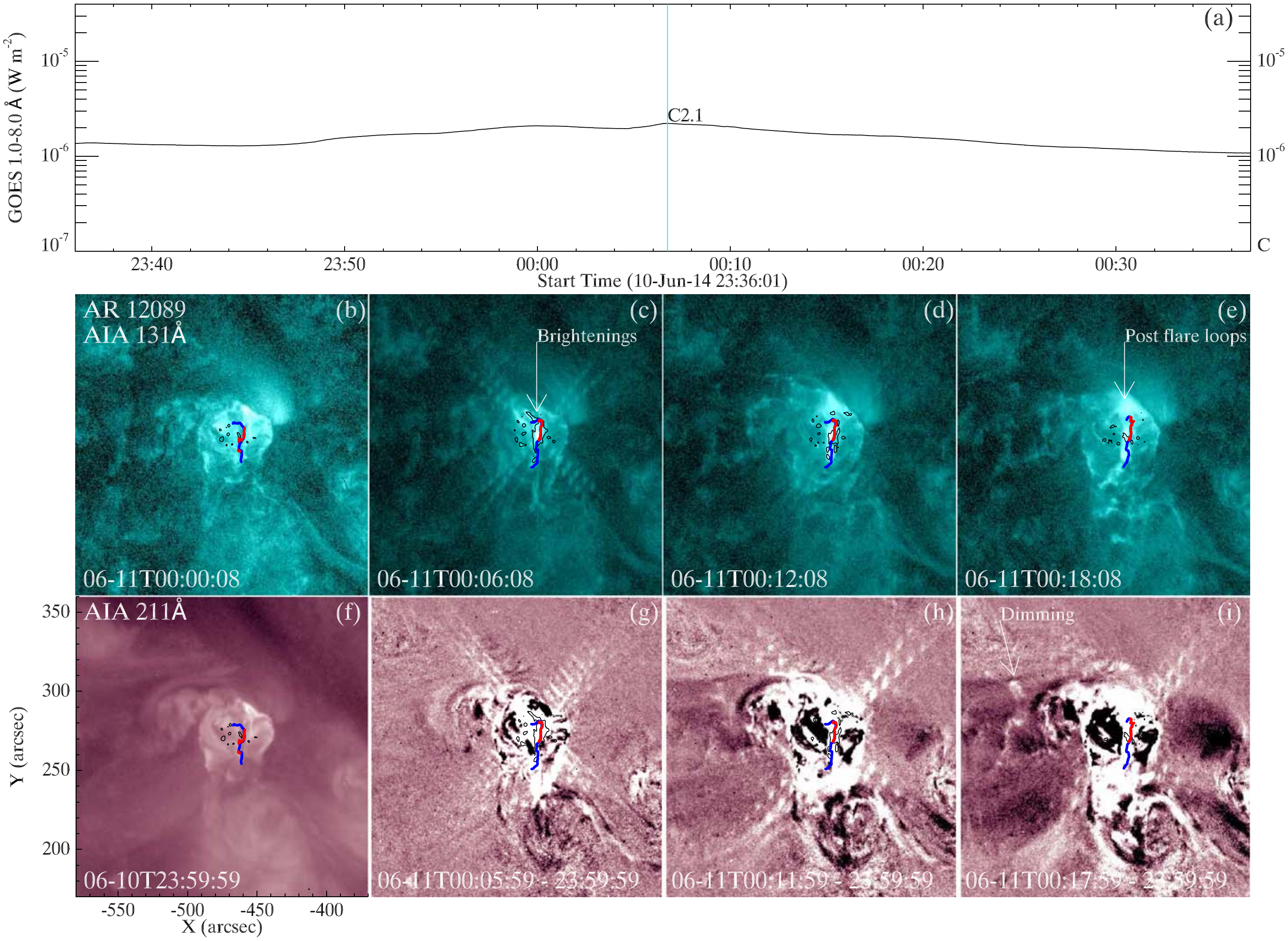

Figure 6. The first major activity that occurred in NOAA AR 12089. Similar layout to Figure 2. Panels (f)–(i) are the base-difference images of the AIA 211 Å passband to show the coronal dimmings during the activity. The blue lines are the cPIL between PB and NA, while the red lines are the collisional parts of the PILs. An animation lasting from 2014 July 11T00:00 to 2014 July 11T00:23. is available online.

(An animation of this figure is available.)

length of the collisional PIL parts obtained on B_r increases from 2.9 to 25.6 Mm, and the mean shear angle remains almost invariant around 60°. For the $B_{\rm los}$ data set, $L_{\rm cPIL}$ also increases from 6.8 to 29.8 Mm, while S remains around 60°. The differences in $L_{\rm cPIL}$ and S in the two data sets are 10.6% and −7.9%, respectively, indicating the increase of $L_{\rm cPIL}$ and decrease of S when changing the data set from B_r to $B_{\rm los}$ in this event.

The first major activity from the AR is a slow CME with a velocity of 387 km s^{-1}, associated with a C2.9 class flare starting from 2012 March 21T12:38 (Figure 10). In both the AIA 131 Å and 304 Å passbands, mass eruption is observed at the source PIL. Flaring ribbons along both sides of the PIL are observed in the AIA 1600 Å passband (black contours in Figure 10), confirming it is the source of the eruption.

3.2.3. The Conjoined sPIL/cPIL in NOAA AR 11776

NOAA AR 11776 transits from Stonyhurst longitude 11°E to 03°E until the flare, with its disk-centered angle changing from 14°.4 to 10°.0. It is composed of two bipoles, A and B, which start to emerge from around 2013 July 18T07:12 (Figure 11) simultaneously. The collisional shearing is case A. The negative polarities of the two bipoles reside close to each other. As emergence proceeds, the conjugated polarities of each bipole separate, and the two negative polarities collide and coalesce with each other. Consequently, no distinct boundary between them could be drawn on the magnetograms. The PIL formed between PB and the group of NA and NB is the active PIL of the AR. On the PIL, collisional signatures appear and grow gradually. It is thus classified as a conjoined sPIL/cPIL. Disappearance of the positive polarities is observed (enclosed in magenta circles in Figure 11), indicating flux cancellation. From the trajectories of the flux-weighted centroids of the polarities (Figure 11(g)) one can see, PA first moves westward and then turns to the northeast. PB moves eastward. Both NA and NB roughly move toward the west, with NB inclining slightly to the north and NA slightly to the south.

Until the flare, the distance between PA and NA increases from 12.3 to 24.6 Mm, and that between PB and NB from 10.7 to 19.6 Mm (Figure 11(h)). The distance between NA and PB changes a little, decreasing slightly from 16.9 to 12.7 Mm, then increasing again to 17.2 Mm. The results confirm the separation between the conjugated polarities, and the collision between PB and the group of NA and NB. The AR is still small with the

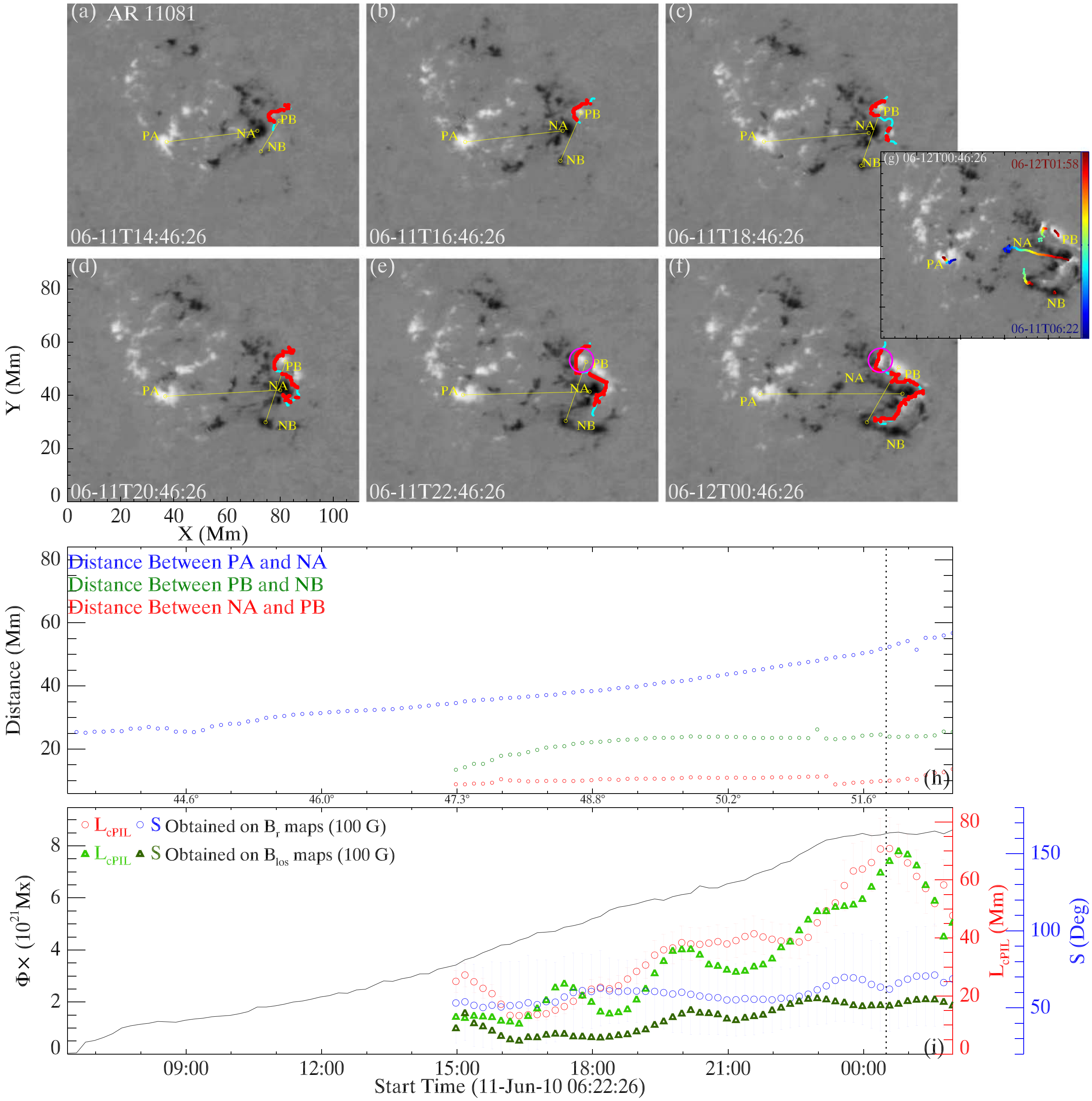

Figure 7. The evolution of NOAA AR 11081. Same layout as Figure 1. An animation of the magnetograms lasting from 2010 July 11T06:22 to 2010 July 12T03:22 is available online.

(An animation of this figure is available.)

unsigned magnetic flux of 2.0×10^{21} Mx (Figure 11(i)). The length of the collisional PIL part obtained on B_r increases from 4.7 to 19.5 Mm, and the mean shear angle increases from 41°.3 to 71°.2. For the $B_{\rm los}$ data set, $L_{\rm cPIL}$ also increases from 3.6 to 18.4 Mm, while S increases from 47°.4 to 71°.6. The difference in $L_{\rm cPIL}$ on the two data sets is −4.4%, and that in S is 4.8%, which are both quite small.

The first major activity from AR 11776 is a CME accompanied by a C2.3 class flare (Figure 12). The CME is ejected with a velocity of around 287 km s^{-1}, with the associated flare starting from around 2013 July 19T00:50 (see Table 1). During the flare, brightenings are observed at the PIL between PB and the group of NA and NB in both the AIA 131 and 211 Å passbands. Moreover, post-flare loops appear along the PIL (Figure 12(d)). Dimmings are observed in the AIA 211 Å passband, verifying the depletion of mass during the CME. The flaring ribbons in the 1600 Å passband (black contours in Figure 12) are observed along the PIL, confirming that it is the source of the eruption.

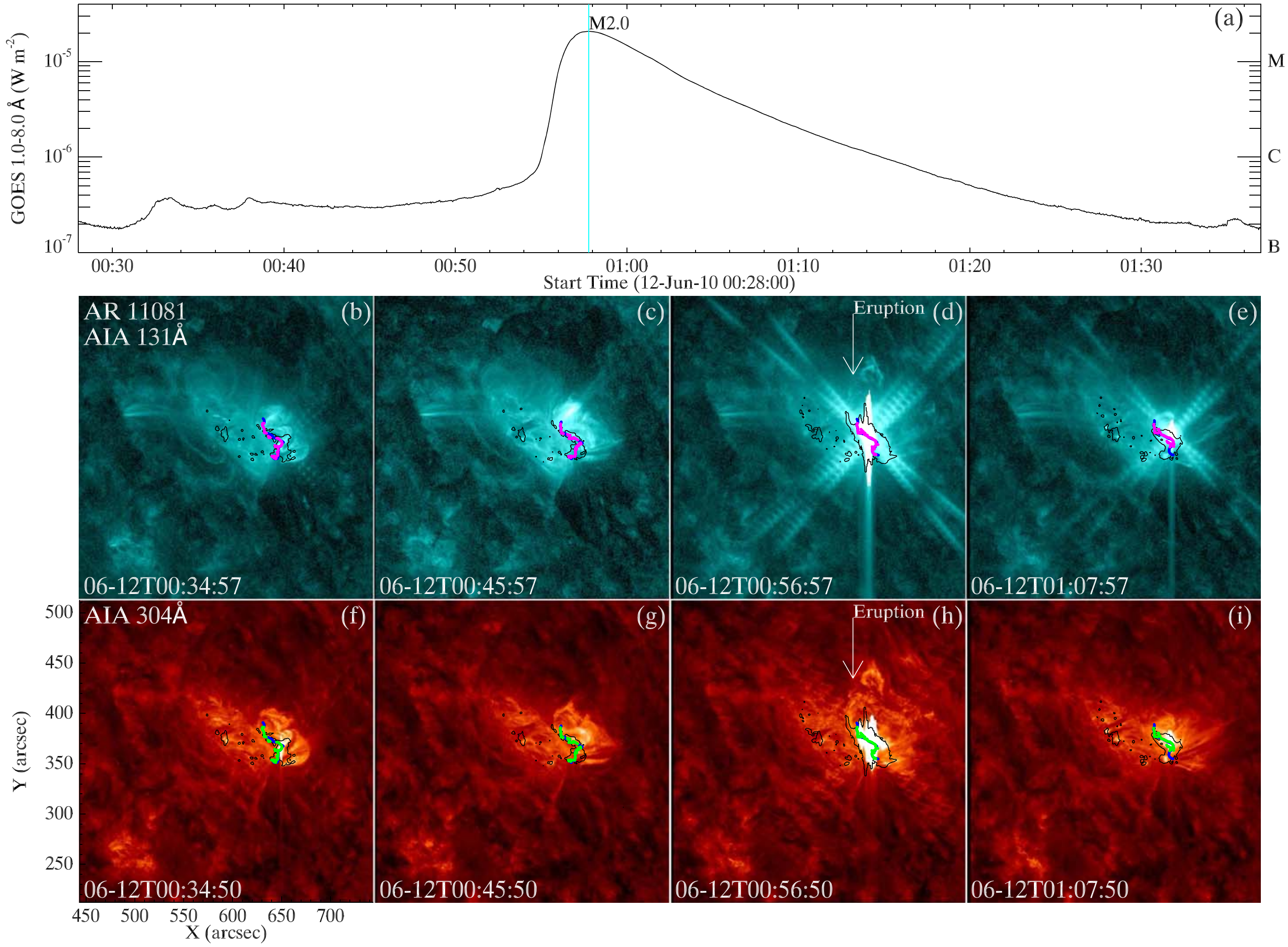

Figure 8. The first major activity that occurred in NOAA AR 11081. Same layout as Figure 2. An animation lasting from 2010 July 12T00:35 to 2010 July 12T01:11 is available online.

(An animation of this figure is available.)

3.3. Examples of the Conjoined sPIL/ePIL

3.3.1. The Conjoined sPIL/ePIL in NOAA AR 11422

NOAA AR 11422 is a bipolar region that starts to emerge from around 2012 February 18T09:58 (Figures 13(a)–(f)). It transits from Stonyhurst longitude 24°E to 11°E until the flare, with the disk-centered angle changing from 33°.2 to 25°.5. An external negative polarity patch (NE) is pre-existing to the north of the bipole. The PIL formed between the positive polarity PA and the negative polarities NA and NE is the active PIL of the AR. Collisional signatures are also observed at the PIL. The collisional PIL part detected on the B_r series at 100 G (red line parts in Figure 13) seems not that significant compared to the entire, longer, PIL (cyan lines in Figure 13). Note that the strength of the magnetic field near the two conjoined sPIL/ePIL is lower than the others, therefore the large thresholds may underestimate their collision. We thus also display the collisional PIL parts detected at 50 G on $B_{\rm los}$ for the sPIL/ePIL case for comparison. It is seen that the collision detected at lower threshold (purple line parts in Figures 13(a)–(f)) is apparently longer than the one detected at higher thresholds (red line parts), mostly occurring between PA and the external NE. Since the active PIL contains a self part between PA and NA and an external part between PA and NE, it is classified as a conjoined sPIL/ePIL.

The trajectories of the flux-weighted centroids of the polarities show that PA moves northeastward while NA moves northwestward, separating from it (Figure 13(g)), which is confirmed by the evolution of the distance between them (Figure 13(h)). From the start of the flux emergence until the flare, the distance between the polarities increases from 28.6 to 43.8 Mm. The unsigned magnetic flux of the AR grows to 3.5×10^{21} Mx (Figure 13(i)). The length and the mean shear angle of the collisional PIL part obtained at 100 G on B_r remain relatively small. The former increases from 3.3 to 10.5 Mm, and the latter increases slightly from 43°.2 to 49°.4. The parameters obtained on $B_{\rm los}$ at 100 G show a similar trend, with $L_{\rm cPIL}$ increasing from 1.1 to 8.2 Mm, and S from 13°.8 to 59°.7. The difference in $L_{\rm cPIL}$ in the two data sets is −8.7%, and that in S is −9.0%. When changing the detection threshold to 50 G, $L_{\rm cPIL}$ is significantly longer (Figure 13(i)), increasing from 3.3 to 34.5 Mm. The shear angle also increases from 37°.2 to 45°.7. The results indicate that the collision in the conjoined sPIL/ePIL in AR 11422 is not trivial.

The first major activity from the AR is a slow CME propagating with a velocity of around 238 km s^{-1},

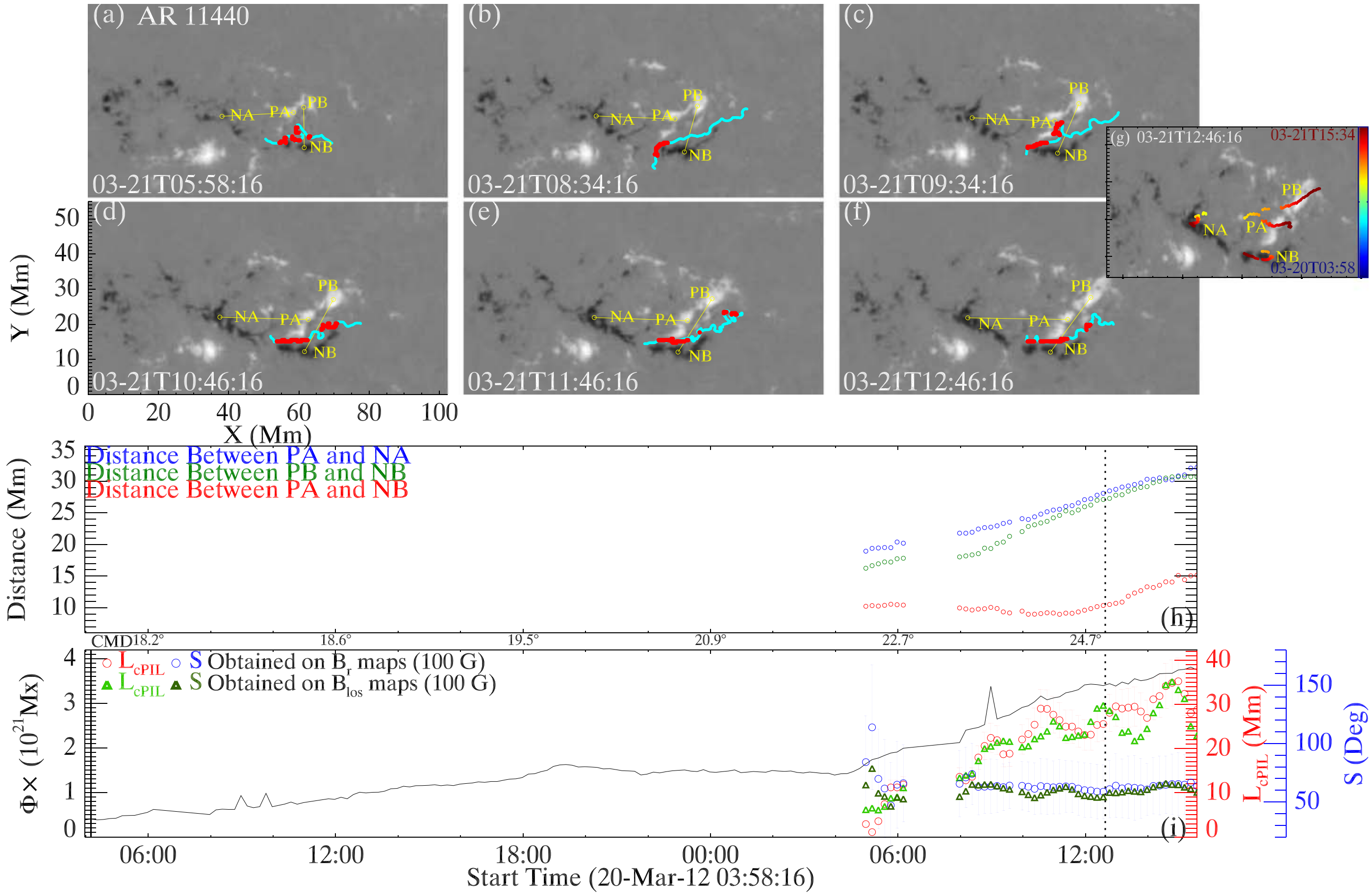

Figure 9. The evolution of NOAA AR 11440. Same layout as Figure 1. An animation of the magnetograms lasting from 2012 March 21T02:58 to 2012 March 21T17:34:16 is available online.

(An animation of this figure is available.)

accompanied by a C1.0 class flare that starts from around 2012 February 19T08:41 (see Table 1). The images in both the AIA 131 Å and 211 Å passbands clearly show that the eruption generates brightenings along the active PIL (Figure 14). Post-flare loops across the PIL are also observed (Figure 14(e)). Furthermore, regions of dimming appear in the 211 Å passband, indicating the mass depletion associated with the CME. Flaring ribbons in the AIA 1600 Å passband also appear along the PIL (black contours in Figure 14), confirming that it is the source of the eruption.

3.3.2. The Conjoined sPIL/ePIL in NOAA AR 11870

NOAA AR 11870 transits from Stonyhurst longitude 14°E to 28°W until the flare, with the disk-centered angle changing from 24°.1 to 32°.5. It is a bipolar region that starts to emerge from around 2013 October 13T06:10 (Figures 15(a)–(f)). A patch of dispersive negative polarity is pre-existing to its south (NE). The PIL between PA and the group of NA and NE is the active PIL of the AR (cyan line in Figures 15(a)–(f)), which is obviously a conjoined sPIL/ePIL. Collisional signatures also appear on the PIL. The one detected at higher thresholds of 100 G (on B_r, red line parts in Figures 15(a)–(f)) is quite short compared to the entire PIL. The one detected at lower thresholds of 50 G (on $B_{\rm los}$, purple line parts) is longer. It is seen that in the early stage of emergence (Figures 15(a)–(c)), a considerable part of the collision occurs between the conjugated PA and NA, while near to the flare (Figures 15(d)–(f) most of the collision occurs between PA and the external NE.

As emergence proceeds, the two conjugated polarities separate (Figure 15(g)). The flux-weighted centroids of the polarities change several times. As a rough guide, PA moves southwestward, while NA moves to the north at first then turns to southeast. Until the flare, the distance between PA and NA increases from 25.0 to 53.4 Mm (Figure 13(h)). The unsigned magnetic flux of the AR grows to 5.1×10^{21} Mx (Figure 15(i)). The length of the collisional PIL part obtained on B_r at 100 G evolves dramatically, increasing from 0.7 to 28.0 Mm, then decreasing to 3.9 Mm. The mean shear angle increases from 63°.0 to 84°.5. The parameters obtained on $B_{\rm los}$ at 100 G show a similar evolutionary trend. $L_{\rm cPIL}$ first increases from 0.7 to 22.8 Mm, then decreases to 2.5 Mm until the flare. S increases from 53°.8 to 99°.7. The difference in $L_{\rm cPIL}$ in the two data sets is −12.3%, and that in S is −1.5%. For the collisional PIL part detected at 50 G on $B_{\rm los}$, $L_{\rm cPIL}$ also evolves dramatically, increasing from 2.2 Mm to as high as 61.5 Mm, then decreasing to 9.5 Mm until the flare, similar to the one obtained at the higher threshold. S increases from around 60°.0 to 82°.5. This indicates that the collision at this sPIL/ePIL is severe in the early phase of emergence, but becomes mild right before the flare.

The first major activity from the AR is a CME with a velocity of 514 km s^{-1}, accompanied by a C1.8 class flare

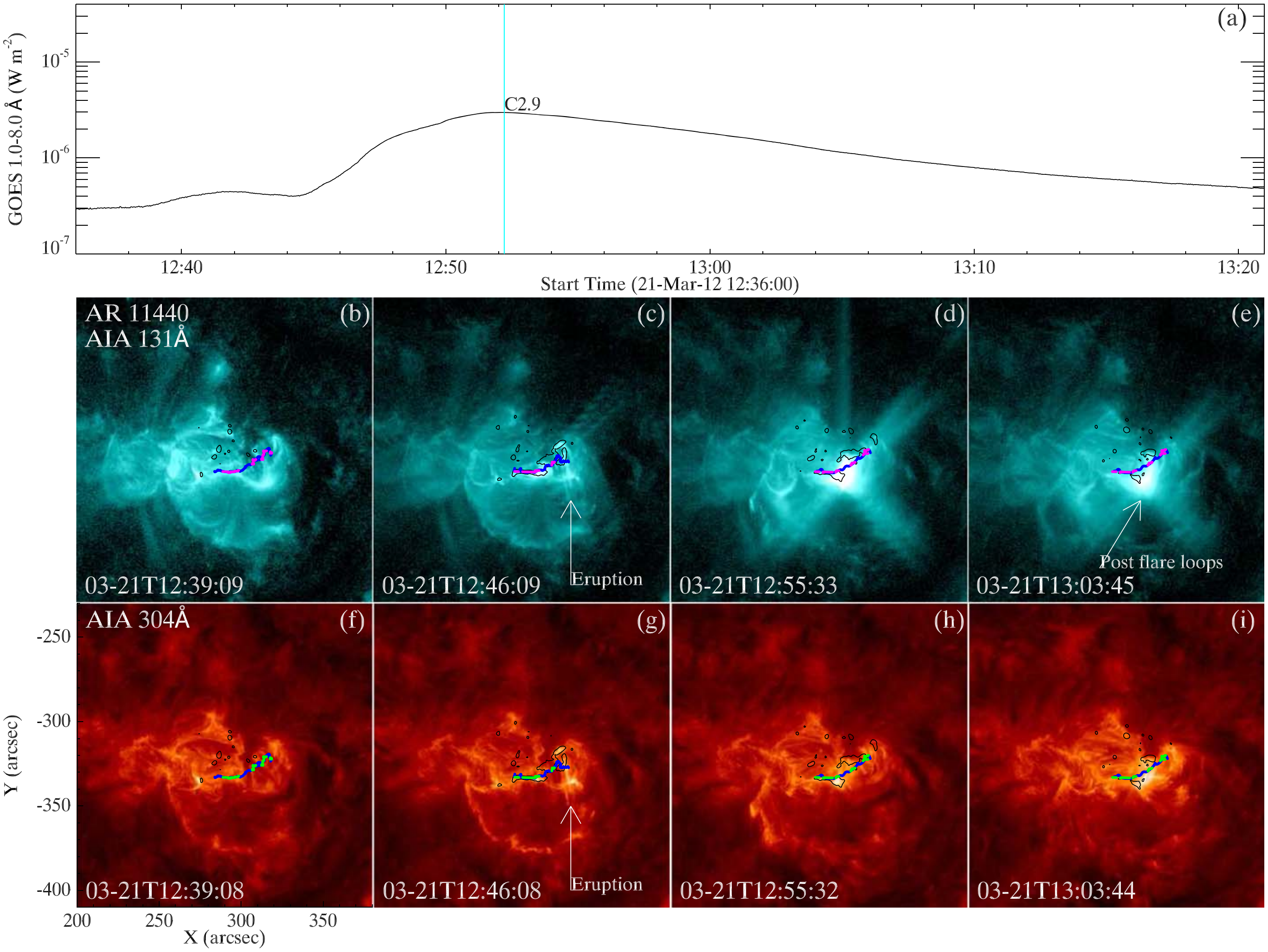

Figure 10. The first major activity that occurred in NOAA AR 11440. Same layout as Figure 2. An animation lasting from 2012 March 21T12:39 to 2012 March 21T13:10:57 is available online.

(An animation of this figure is available.)

starting from 2013 October 16T15:03 (Figure 16). In both the AIA 131 Å and 211 Å passbands, brightenings occur along the PIL. After the flare, post-flare loops across the PIL are observed (Figure 16(e)). Dimming regions appear in the 211 Å passband, which indicate the mass depletion during the CME. The flaring ribbons in the 1600 Å passband occur along both sides of the PIL, confirming that it is the source of the eruption.

3.4. Correlation between the Intensity of the Activities and $\overline{L}_{\rm cPIL}$ and $\overline{S}$

We further inspect the properties of all active PILs and their correlation with the intensity of the activities. Specifically, we check the correlation between GOES 1–8 Å peak flux (F) and the mean length ($\overline{L}_{\rm cPIL}$) and mean shear angle ($\overline{S}$) of the collisional PIL, which are averaged over a given duration prior to the activities. Durations of 1, 3, and 5 hr are used for the averaging. The analysis is performed at various thresholds on the two data sets to avoid bias (see also Section 2).

Figure 17 displays scatter diagrams between F and $\overline{L}_{\rm cPIL}$ obtained on the B_r series. It is seen that in general, $\overline{L}_{\rm cPIL}$ of the collisional parts of the PILs detected at lower threshold is longer than that detected at higher threshold. The values calculated from 100 and 125 G are close, with the former being around 4 Mm longer than the latter. Those calculated from 150 G are around 7 Mm shorter than those from 125 G, but are close to (around 2 Mm higher than) those from 175 G. For a fixed threshold, $\overline{L}_{\rm cPIL}$ computed over different durations shows no significant difference, although the value decreases slightly as the duration increases. Overall, there is a relatively nontrivial correlation between the magnitude of the flares and the length of the collisional parts of the PILs, which is established for all thresholds and durations. The Pearson correlation coefficients are not small, ranging from 0.63 to 0.75 with the confidence levels all greater than 99%. This indicates that more intense activities tend to originate from the longer collisional PILs.

We choose the values calculated at the threshold of 100 G and duration of 3 hr for interpretation (Figure 17(b)). A linear fitting to the scatter plot gives the relation $\log(F) = 0.013 \times \overline{L}_{\rm cPIL} - 5.63$ (the black solid line). $\overline{L}_{\rm cPIL}$ of different ARs are rather scattered. The collisional parts of the two conjoined sPIL/ePIL are the shortest, measuring 4.3 and 11.7 Mm. Those of the six conjoined sPIL/cPIL are larger overall, ranging from 20.0 to 61.0 Mm. $\overline{L}_{\rm cPIL}$ of the 11 cPILs are the largest, ranging from 12.9 to 87.5 Mm. In general, the average of all $\overline{L}_{\rm cPIL}$ is 41.8 Mm (the vertical dashed line in

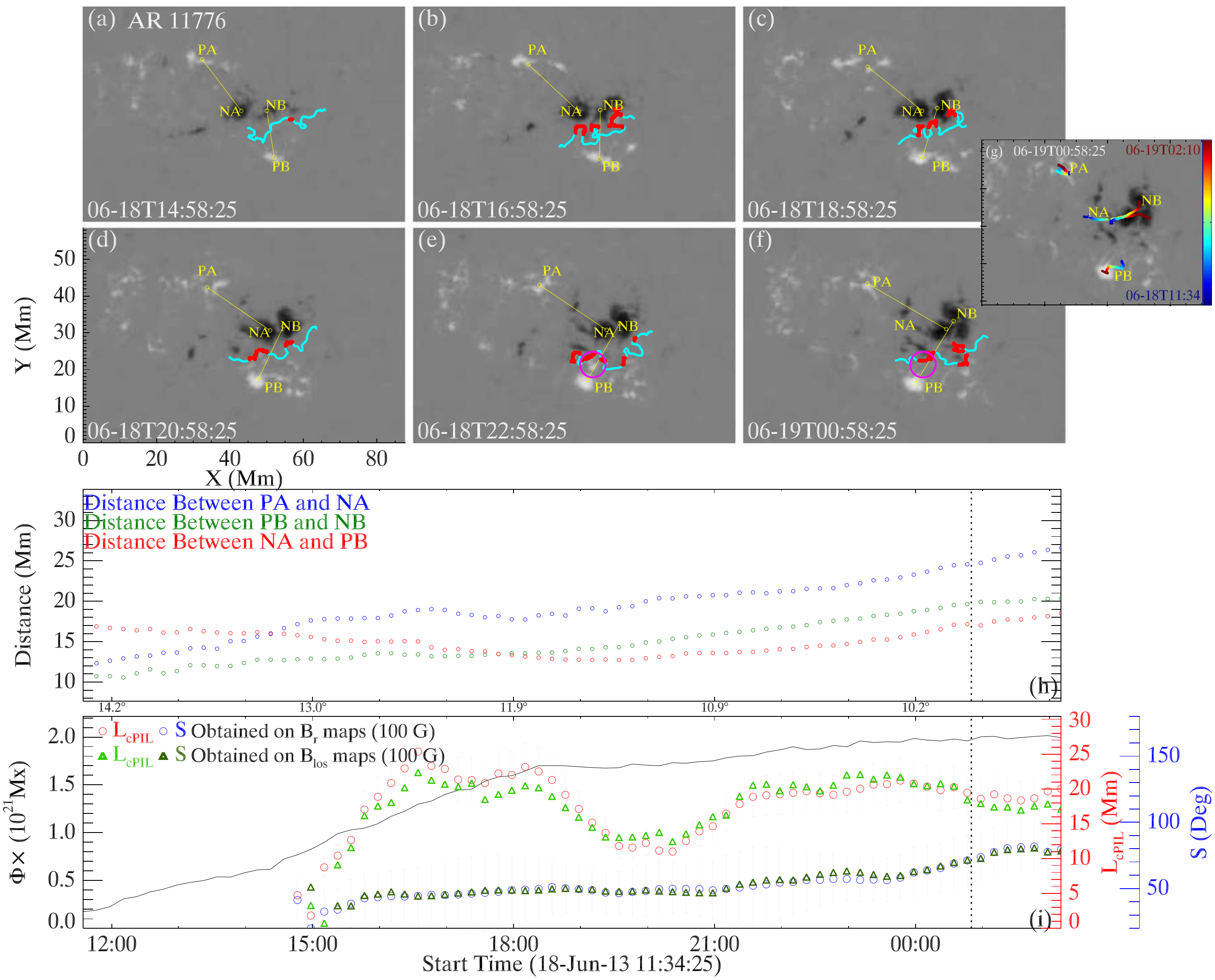

Figure 11. The evolution of NOAA AR 11776. Same layout as Figure 1. An animation of the magnetograms lasting from 2013 July 18T11:34 to 2013 July 19T03:46 is available online.

(An animation of this figure is available.)

Figure 17(b)), and 68% (13/19) of the $\overline{L}_{\mathrm{cPIL}}$ fall in the range 18–65.6 Mm (the shaded region in Figure 17(b)), which represents one standard deviation (σ) below and above the average. Considering that F is positively correlated to $\overline{L}_{\mathrm{cPIL}}$, taking the averaged lower cutoff value for $\overline{L}_{\mathrm{cPIL}}$ (18 Mm here) as a reference value may be useful for assessing the significance of the collision, and thus evaluating the productivity of the AR. It is seen that except for the two conjoined sPIL/ePIL and one cPIL in AR 12089, 84% (16/19) of the $\overline{L}_{\mathrm{cPIL}}$ are above the reference value.

Note that all of the activities occur within the region $\Theta \leqslant 60^{\circ}$ (see Table 1), with nine cases close to the disk center (having $\Theta \leqslant 30^{\circ}$, each marked by a "+" symbol in a circle in Figure 17). As discussed in Section 2, the criterion $\Theta \leqslant 60^{\circ}$ could ensure relatively high signal-to-noise ratio of the data, but is still less strict than $\Theta \leqslant 30^{\circ}$ since both data sets suffer from the least uncertainty near the center. We thus further perform a correlation analysis on the nine near-center cases particularly (shown in olive in Figure 17). It is seen that there is still relatively nontrivial correlation between F and $\overline{L}_{\mathrm{cPIL}}$. The correlation coefficients range from 0.62 to 0.85, and are very close to those obtained from the full sample at the thresholds of 100 and 150 G, and slightly higher at the thresholds of 125 and 175 G. The confidence levels of the correlations are lower than those from the full sample, ranging from 92.3% to 99.6%, which may result from the smaller sample size of nine cases. In short, the trend that more intense activities tend to originate from the PILs with longer collisions still exists when only considering the cases having less noisy data.

One may also question whether the relatively nontrivial correlations may be largely determined by the two conjoined sPIL/ePIL cases, since they have the shortest $\overline{L}_{\mathrm{cPIL}}$ as well as the smallest flare. In order to check this possibility, we further analyze the correlation on a sample excluding the two cases (shown in purple in Figure 17). It is seen that the Pearson correlation coefficients are smaller than those from the full sample, decreasing by around 0.1, but are still relatively nontrivial, ranging from 0.5 to 0.67. The decrease in the coefficients suggests that the two sPIL/ePIL cases do bias the correlation. Moreover, since there are only two sPIL/ePIL

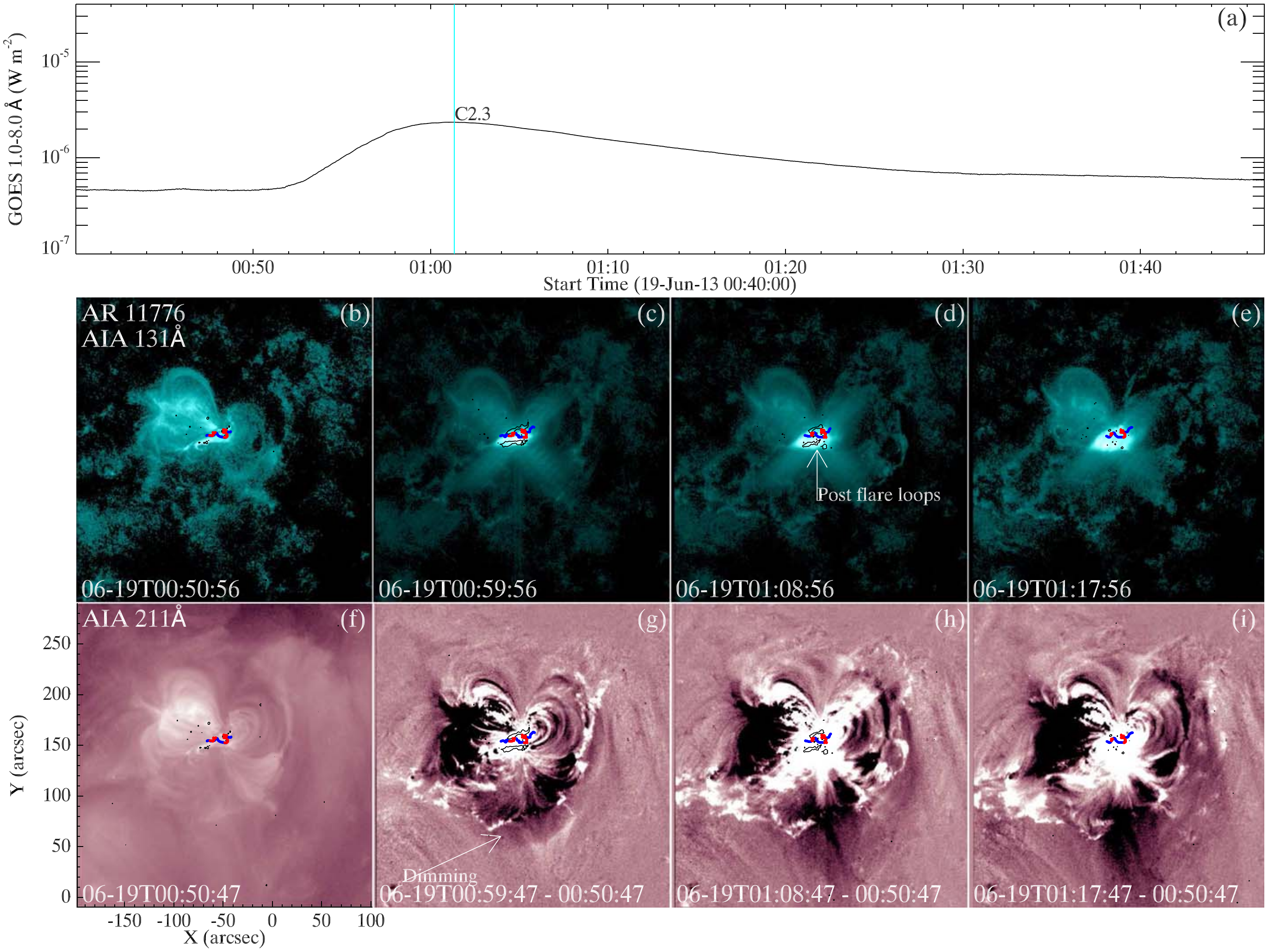

Figure 12. The first major activity that occurred in NOAA AR 11776. Same layout as Figure 6. An animation lasting from 2013 July 19T00:51 to 2013 July 19T01:21 is available online.

(An animation of this figure is available.)

cases, we are not able to draw precise conclusion about how much this kind of case can affect the correlation. We can only see that the correlation coefficients are not small even after excluding the two cases, which still indicates the trend that more intense activities tend to originate from PILs with greater collisional length.

The $\overline{L}_{\mathrm{cPIL}}$ obtained on the B_{los} data set show a similar distribution (Figure 18). In general, $\overline{L}_{\mathrm{cPIL}}$ decreases as the detection threshold increases, by about 7 Mm per 25 G on average. For a fixed threshold, $\overline{L}_{\mathrm{cPIL}}$ calculated from longer durations are slightly lower. Taking the values obtained at the threshold of 100 G and a duration of 3 hr as an example (Figure 18(h)), the mean value of $\overline{L}_{\mathrm{cPIL}}$ is 42.8 Mm. Then 84% (16/19) of the $\overline{L}_{\mathrm{cPIL}}$ are longer than 18.8 Mm (1σ below the average), excepting only the two conjoined sPIL/ePIL and a cPIL in AR 12089. The two lower cutoff values obtained on both B_r and B_{los} data sets are quite close; we thus take 18 Mm as a reference value when assessing the intensity of the collision. Relatively nontrivial correlation still exists between F and $\overline{L}_{\mathrm{cPIL}}$ for all thresholds and durations on B_{los}. The correlation coefficients range from 0.56 to 0.82 with a confidence level higher than 98%. When only considering the nine cases near the disk center, there is also relatively nontrivial correlation. The correlation coefficients are slightly lower than on the full sample at the smaller threshold (50–100 G), and slightly higher at the larger threshold (125–175 G), ranging from 0.51 to 0.91. The confidence levels are lower, ranging from 83.8% to 99.9%, which may be because that the sample size of nine cases is smaller. When excluding the two sPIL/ePIL cases, the correlation coefficients also decrease (by around 0.02 to 0.1), but are still nontrivial, ranging from 0.54 to 0.77. This also indicates that the two sPIL/ePIL cases do bias the correlation, but do not seem to significantly affect the trend indicated by the correlation that more intense activities tend to originate from PILs with greater collisional length.

Overall, the results obtained at larger thresholds ($\geqslant$100 G, Figures 18(g)–(r)) on B_{los} correlate well with those from the B_r data set. For those obtained from lower thresholds (50 and 75 G, Figures 18(a)–(f)), the correlation, with coefficients ranging from 0.56 to 0.71, becomes weaker but still cannot be ignored. The other difference is that $\overline{L}_{\mathrm{cPIL}}$ of one conjoined sPIL/ePIL from AR 11422 becomes significantly larger, e.g., increasing from 10.0 to 48.0 Mm when the threshold changes from 100 to 50 G for an averaging duration of 3 hr (see also in Section 3.3). The increase in $\overline{L}_{\mathrm{cPIL}}$ again indicates that a lower threshold may be more appropriate for the sPIL/ePIL cases

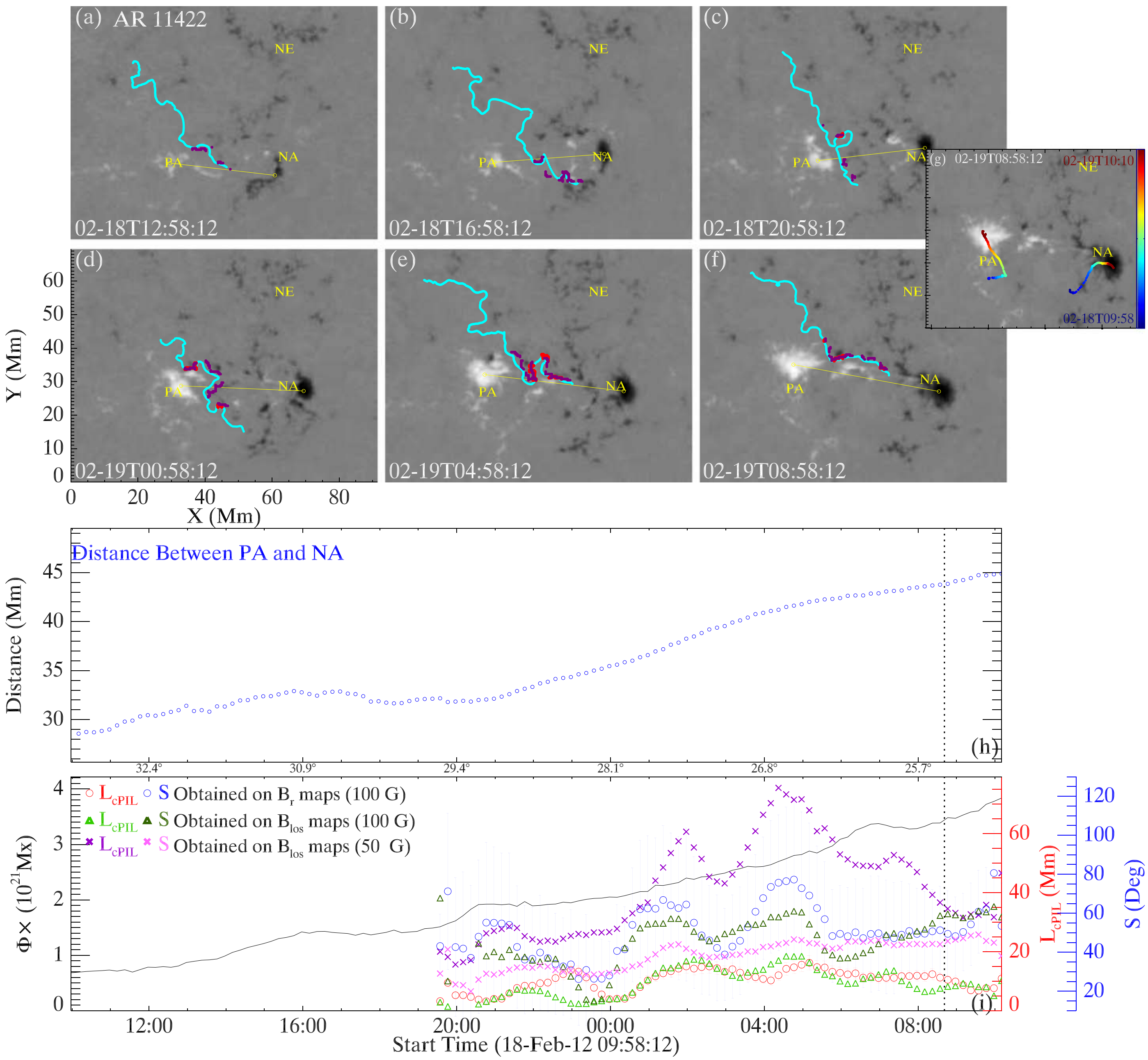

Figure 13. The evolution of NOAA AR 11422. Similar layout to Figure 1. NE denotes the external negative polarity. The collisional PIL part detected at the threshold of 50 G on the $B_{\rm los}$ data set is overplotted on the B_r magnetograms for comparison (in purple). Its $L_{\rm cPIL}$ and S are also shown in panel (i). There is a slight inconsistency between the spatial locations of the purple line and the cyan line (or red line), which may result from the difference between the corrected $B_{\rm los}$ and B_r. An animation of the magnetograms lasting from 2012 February 18T09:58 to 2012 February 19T11:22 is available online.

(An animation of this figure is available.)

when detecting their collision. The correlation obtained on the $B_{\rm los}$ data set also supports the idea that there is a trend whereby more intense activities tend to originate from the PILs with longer collisional length.

The correlations between F and the mean shear angle $\overline{S}$ calculated from both data sets at all thresholds and durations show no essential difference. We thus show the scatter diagram between F and $\overline{S}$ detected at 100 G and averaged over 3 hr in Figure 19. For the B_r data set, the average of $\overline{S}$ is around 62°. About 78.9% of $\overline{S}$ fall into the range from 50°.8 to 72°.7 (1σ below and above the average). Taking the lower cutoff value (50°, around 1σ below the average) as a reference, it is found that except for one conjoined sPIL/cPIL in NOAA AR 11762, which has $\overline{S}$ of 36°.1, the rest of the PILs all have $\overline{S}$ very close to or larger than that. For the $B_{\rm los}$ data set, the mean $\overline{S}$ is around 57°, close to that from B_r. However, the lower cutoff value (around 43°) is lower. This may be because that $\overline{S}$ for $B_{\rm los}$ is also calculated using the vector field but on the collisional PIL part detected on the $B_{\rm los}$ series, which may slightly deviate from the PIL detected on B_r. Except for $\overline{S}$ of AR 11899, which is 32°, the rest are all very near to or significantly larger than the lower cutoff value. This result suggests that significant shear has built up at the collisional parts of almost all active PILs prior to the eruptions. The magnitude of the flares exhibits

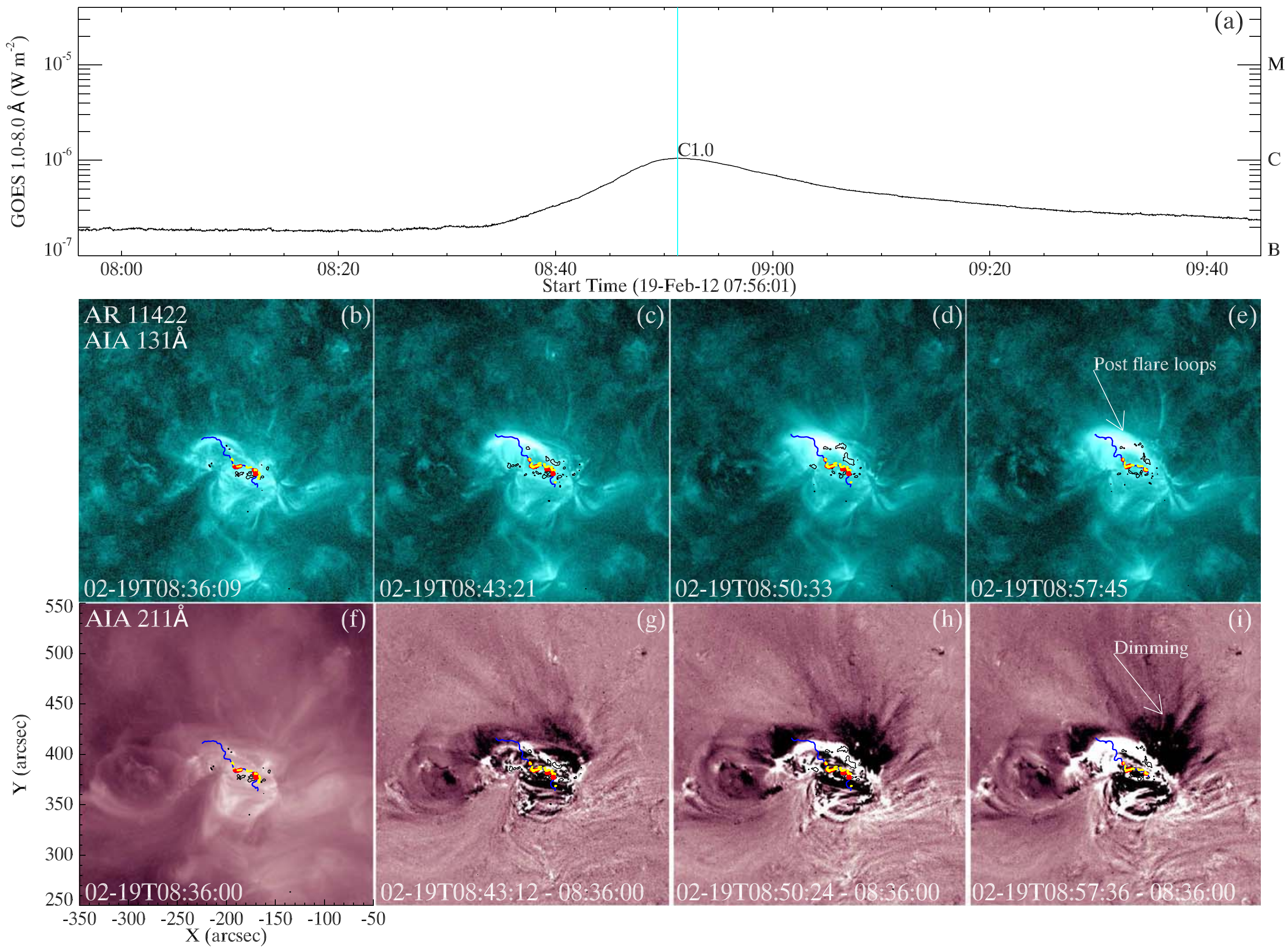

Figure 14. The first major activity that occurred in NOAA AR 11422. Similar layout to Figure 12. The collisional PIL part detected at the threshold of 50 G on $B_{\rm los}$ data set is also overplotted for comparison (in yellow). An animation lasting from 2012 February 19T08:36 to 2012 February 19T09:09 is available online.

(An animation of this figure is available.)

no correlation to $\overline{S}$. We also find no clear correlation between the CME velocities and $\overline{L}_{\rm cPIL}$ and $\overline{S}$, so the results are not shown here.

4. Discussion and Conclusion

In this work, by tracking 19 ARs from the beginning of their emergence until they produce their first major activities, we investigate the formation and properties of the active PILs, i.e., the source PILs of the eruptions. We find that none of the active PILs is simply formed by an individual bipole. In contrast, all of them contain non-self PIL parts. We further find that the PILs can be classified into three types: there are 11 cPILs formed due to collision between different bipoles, six conjoined sPIL/cPIL, which contain the self PIL parts and collisional PIL parts, and two conjoined sPIL/ePIL, which are composed of the self PIL parts and external PIL parts. Moreover, we find that the magnitude of the flares is positively correlated with the length of the collisional parts of the active PILs, which holds on both B_r and $B_{\rm los}$ data sets for all thresholds and averaging durations we investigated.

For the 11 cPILs, collision between nonconjugated polarities of opposite sign develops at all of the PILs prior to the first major activities of the ARs. Observations reveal that the collision accompanied by shearing and flux cancellation is driven by the self-separation of different bipoles when they emerge, which is consistent with the "collisional shearing" scenario proposed by Chintzoglou et al. (2019). The length of the collisional parts clearly shows a trend of increasing from the start of emergence to the onset of activity, while the non-potential shear angles also show a trend of increasing, although not so dramatic, further supporting the ongoing collisional shearing. Taking the collisional lengths detected on the B_r series at 100 G and averaged over 3 hr (prior to the flare) as an example, 10 of them are longer than the reference value of a significant collision (18 Mm).

For the six conjoined sPIL/cPIL, collision also develops and grows at part of the PILs prior to the activities, with shearing and flux cancellation observed. All of the averaged collisional lengths are longer than 18 Mm. In the ARs containing this type of PIL, collision may occur not only between nonconjugated polarities of opposite sign, but also between polarities of the same sign of different bipoles. This kind of collision may further shear the field lines by moving their footpoints. For example, in the sPIL/cPIL case of AR 11776, the negative polarity NA pushes another negative polarity NB to the west,

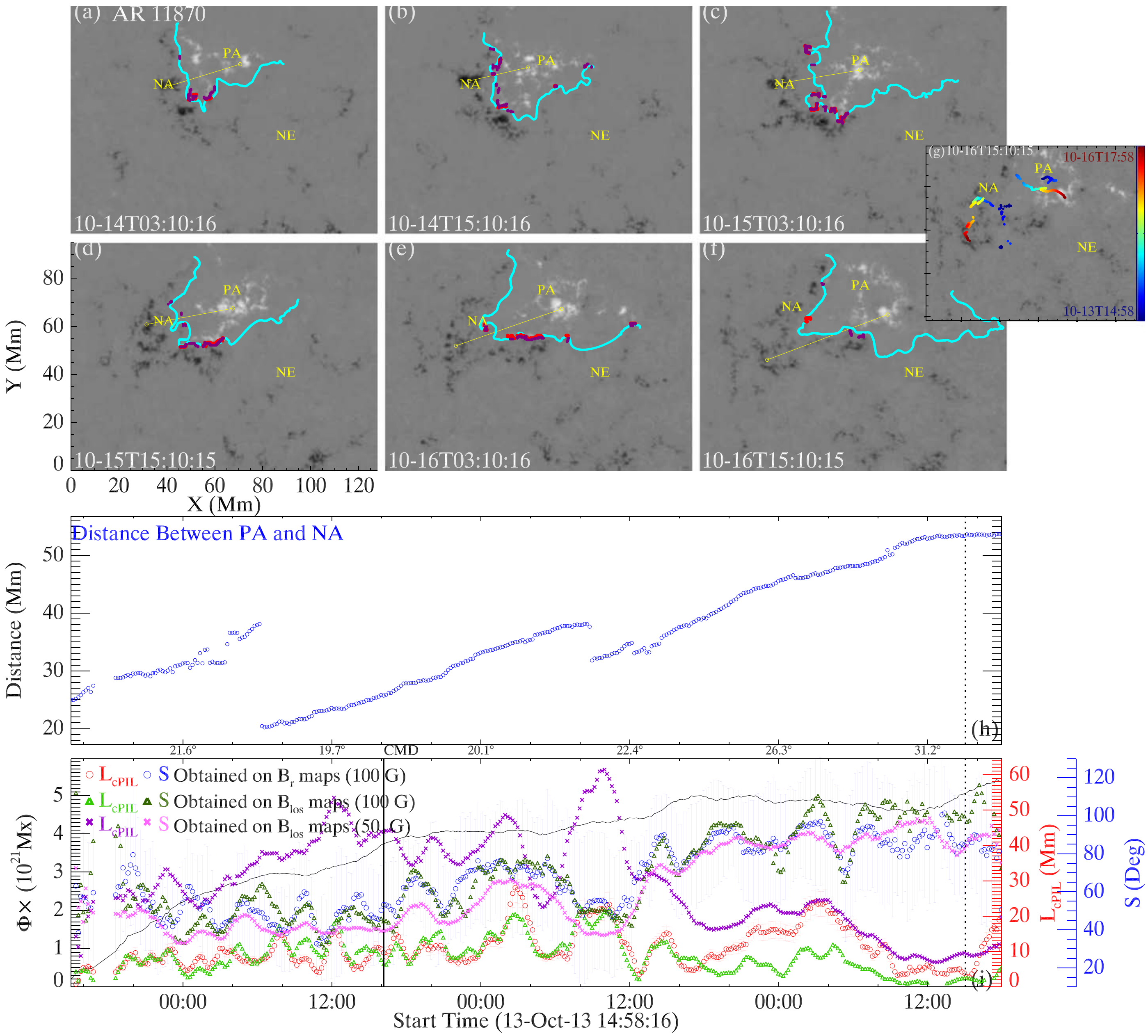

Figure 15. The evolution of NOAA AR 11870. Same layout as Figure 13. An animation of the magnetograms lasting from 2013 October 13T06:10 to 2013 October 16T17:58 is available online.

(An animation of this figure is available.)

which makes NB deviate from its original northward direction, and it can apparently shear the field lines connecting NB and PB. This indeed also is a kind of photospheric motion (see also in Section 1) driven by the collision.

Collision signatures are also observed for the two conjoined sPIL/ePIL. The collisional length is short at the threshold of 100 G. Considering that the magnetic field of the two ARs is not as strong as others, it might be more appropriate to use lower thresholds (e.g., 50 G) on low-noise $B_{\rm los}$ when detecting their collision. When lowering the threshold to 50 G, the collision length of AR 11422 becomes significantly longer until the flare. That of AR 11870 evolves dramatically, being longer at the early phase of emergence and shorter near to the flare. As there are only two sPIL/ePIL cases, we cannot draw a general conclusion on the collision feature of this type of PIL. We have strictly followed the criteria (see Section 2) when selecting the cases from the list of 423 emerging ARs in Kutsenko et al. (2019). As also mentioned in Chintzoglou et al. (2019), the criteria of "emerging and producing major eruptions on the visible disk" are strict and thus have screened out most of the cases. The few sPIL/ePIL cases here are more likely to be an indicator of how often such cases occur.

Overall, for all active PILs we studied, collisional signatures are found to develop prior to the first major activities of the ARs, with 16 of them having averaged collisional length longer than 18 Mm. Here we define 18 Mm (detected at 100 G) as a reference value when assessing the significance of the collision, while the reference value in Chintzoglou et al. (2019) is defined as 40 Mm. Nevertheless, the latter is obtained based on two large, productive ARs, while 18 Mm here is calculated as 1σ

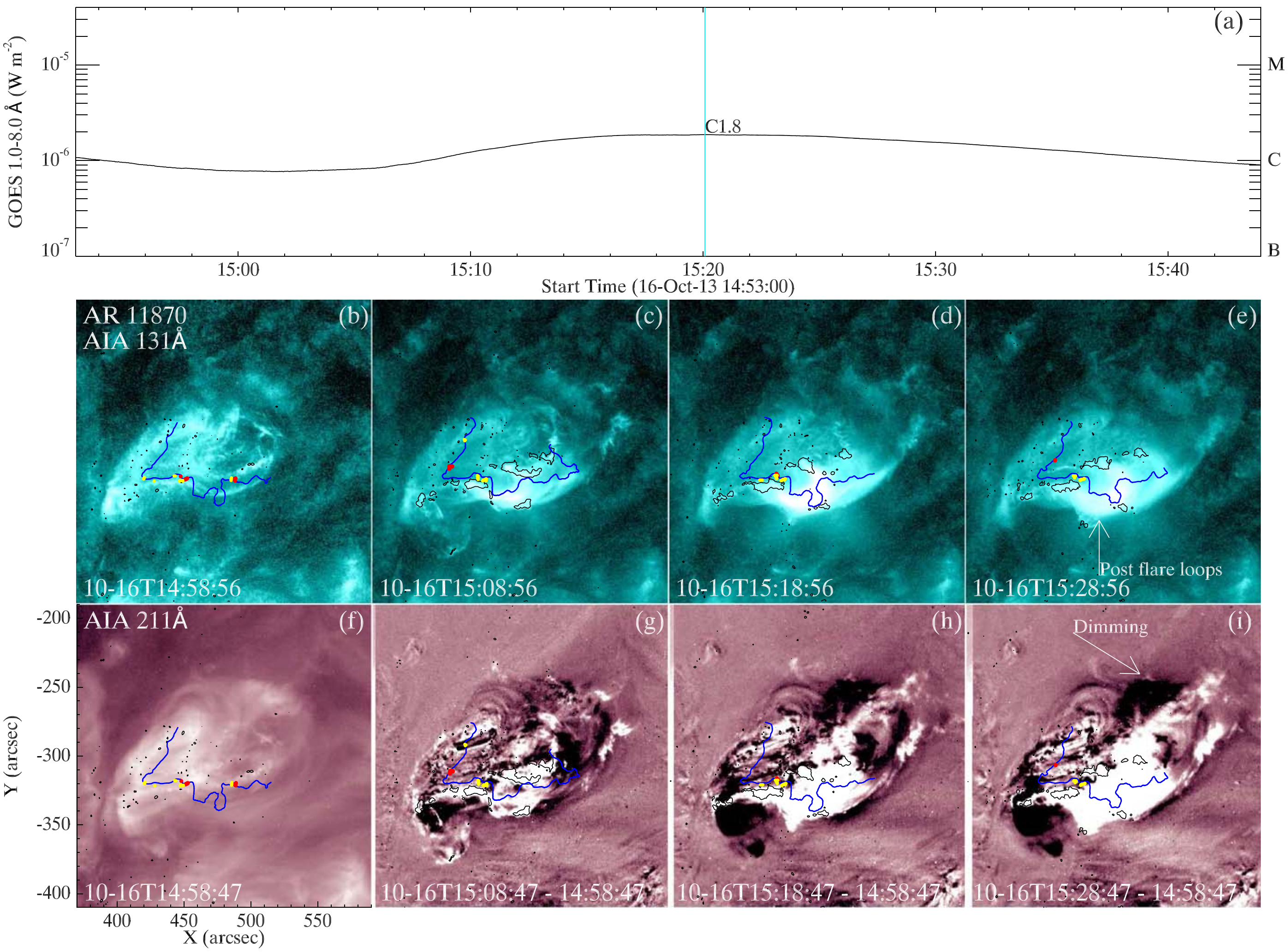

Figure 16. The first major activity that occurred in NOAA AR 11870. Same layout as Figure 12. An animation lasting from 2013 October 16T14:58 to 2013 October 16T15:43 is available online.

(An animation of this figure is available.)

below the averaged collisional length of all active PILs, which are obtained from 19 ARs of various sizes. Thus the two values may not be in conflict, and the value of 18 Mm may be more general.

Note that 18 Mm is just a reference from a statistical perspective. For the three cases that have $\overline{L}_{\rm cPIL}$ shorter than 18 Mm, the small collision at the cPIL one in AR 12089 more likely results from the small size of the AR (around 1.2×10^{21} Mx) since the first major activity occurs only 4 hr after the onset of emergence. The collision is relatively significant for the small AR, playing an important role in driving the eruption. For the conjoined sPIL/ePIL one in AR 11422, the collision before the flare, which also mainly occurs between the nonconjugated polarities, increases to as long as 48 Mm when the detection threshold is lowered to 50 G, indicating that the collision is rather significant. For the other one, i.e., the conjoined sPIL/ePIL in AR 11870, the collisional length before the flare is short (below 10 Mm) even at the lower threshold, but is rather significant (with $L_{\rm cPIL}$ as high as 60 Mm) in the early phase of emergence. Different from the other ARs, a considerable part of the early collision in AR 11870 occurs between the conjugated polarities (e.g., Figure 15(b)), which may result from the small moving dipoles (the conjugated polarities of which are very close) during the emergence. The early collision may have transferred the emerging field higher into the corona, and it may interact with other higher, pre-existing magnetic field, playing a role in producing the eruptions. A similar scenario is discussed in Schmieder et al. (2014, and references therein).

The positive correlation between the magnitude of the flares and the length of the collisional parts of the PILs suggests that the more intense activities tend to originate from the longer collisional PILs, further suggesting that the collision plays an important role in generating the large activities. Considering that the field at almost all collisional PILs is significantly sheared before the eruptions, the longer collisional PILs indicate that more sheared magnetic flux is involved in the cancellation, thus a larger amount of magnetic free energy may be available to consume during the eruptions.

As the flares and CMEs are suggested to be closely related to the eruptions of the magnetic flux ropes (e.g., Shibata et al. 1995), their source locations may give hint to the origin of the coronal flux ropes. For the two generally accepted scenarios of the formation of coronal flux ropes (Cheng et al. 2017, and reference therein), the bodily emergence from the solar interior should produce a bipolar region on the photosphere (e.g., Fan

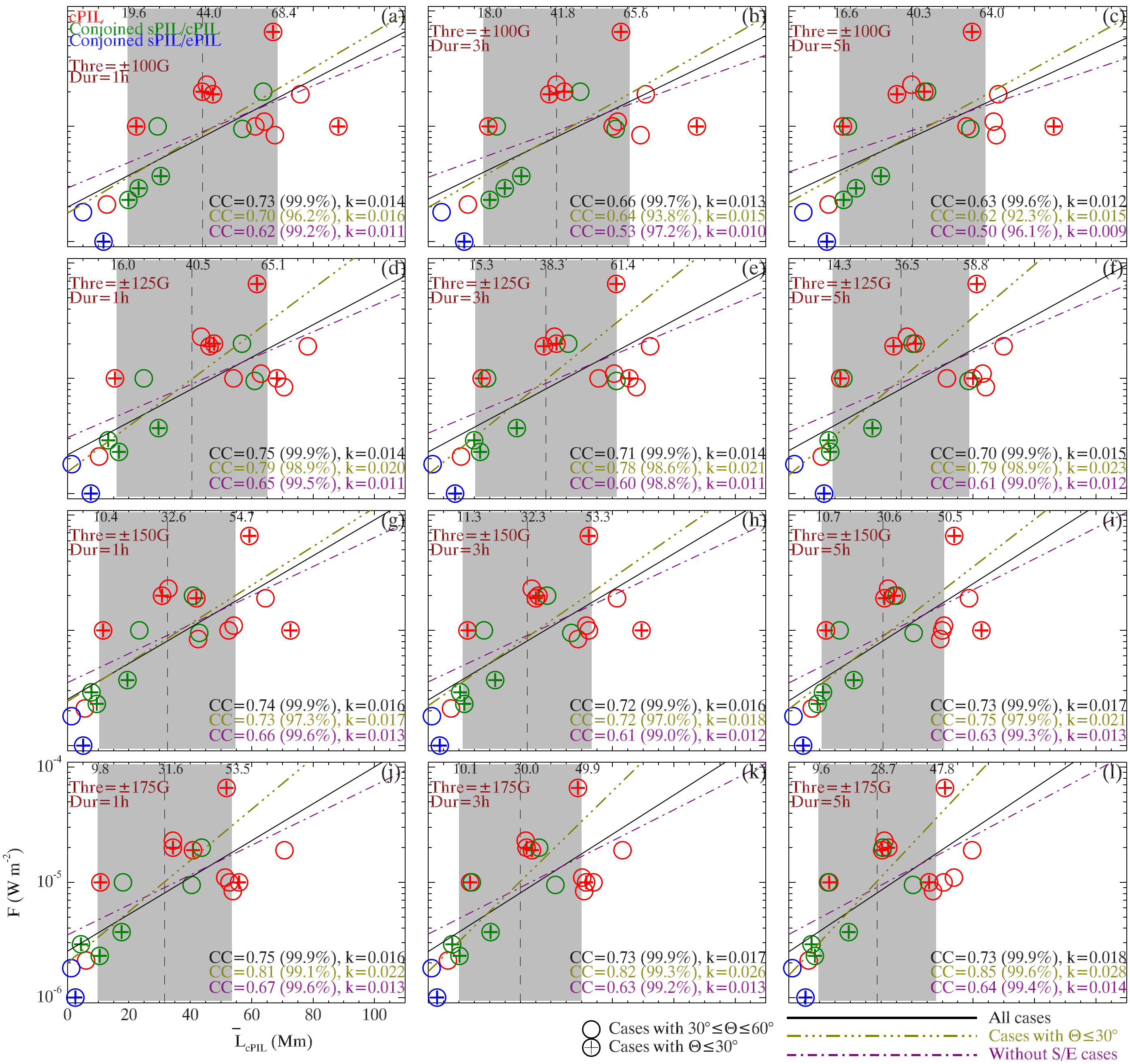

Figure 17. Scatter plots of the mean length of the collisional part of the PIL ($\overline{L}_{\rm cPIL}$) obtained from the B_r data set for various thresholds and averaging durations vs. the GOES 1–8 Å flux (F). For each AR, $\overline{L}_{\rm cPIL}$ is averaged over the given durations prior to its first major activity. The term "Thre" indicates the threshold of the cPIL detection. "Dur" indicates the duration prior to the activities within which the averaging is done. The red circles show the parameters of the cPILs. The green ones are for the conjoined sPIL/cPIL and the blue ones are for the conjoined sPIL/ePIL. The cases having $\Theta \leqslant 30°$ are further marked by the "+" sign in circles. The black solid lines show the result of a linear fitting between $\overline{L}_{\rm cPIL}$ and the logarithmic GOES flux for all cases, with the Pearson correlation coefficient CC and corresponding confidence level, and the slope k shown at the bottom right. The purple dashed–dotted lines show the linear fitting results on the sample excluding the two conjoined sPIL/ePIL cases. The olive dashed–dotted lines show the linear fitting results on the cases with $\Theta \leqslant 30°$. The vertical dashed line in (a) indicates the average of all $\overline{L}_{\rm cPIL}$, with the shaded region covering between one standard deviation (of all $\overline{L}_{\rm cPIL}$) below and above the average. The value of the average and the range of the shaded region are shown on the upper axis. The vertical dashed lines and the shaded regions in the other panels have the same meaning.

& Gibson 2004), while formation in the solar atmosphere usually does not support a simple bipole configuration. In the two productive ARs in Chintzoglou et al. (2019), none of the eruptions originated from the self PIL of a single bipole. The authors thus suggested that no flux rope formed or emerged above the sPIL, and the bodily emergence of flux rope may be rare. In our sample, the lack of activities originating from the single sPIL also supports this point. It is also consistent with other reported observations, in which the filament (a proxy of the flux rope) formed above the self PIL is found to be rare (Mackay et al. 2008).

To summarize, in all of the emerging ARs we studied, the collision develops at the active PILs prior to the first major activities from the ARs, and in at least 84% (16 of 19) of them, the collisional shearing is quite significant. Furthermore, the magnitude of the flares is positively correlated with the length of the collisional parts of the PILs. From the statistical perspective, the results consolidate that the bipole–bipole

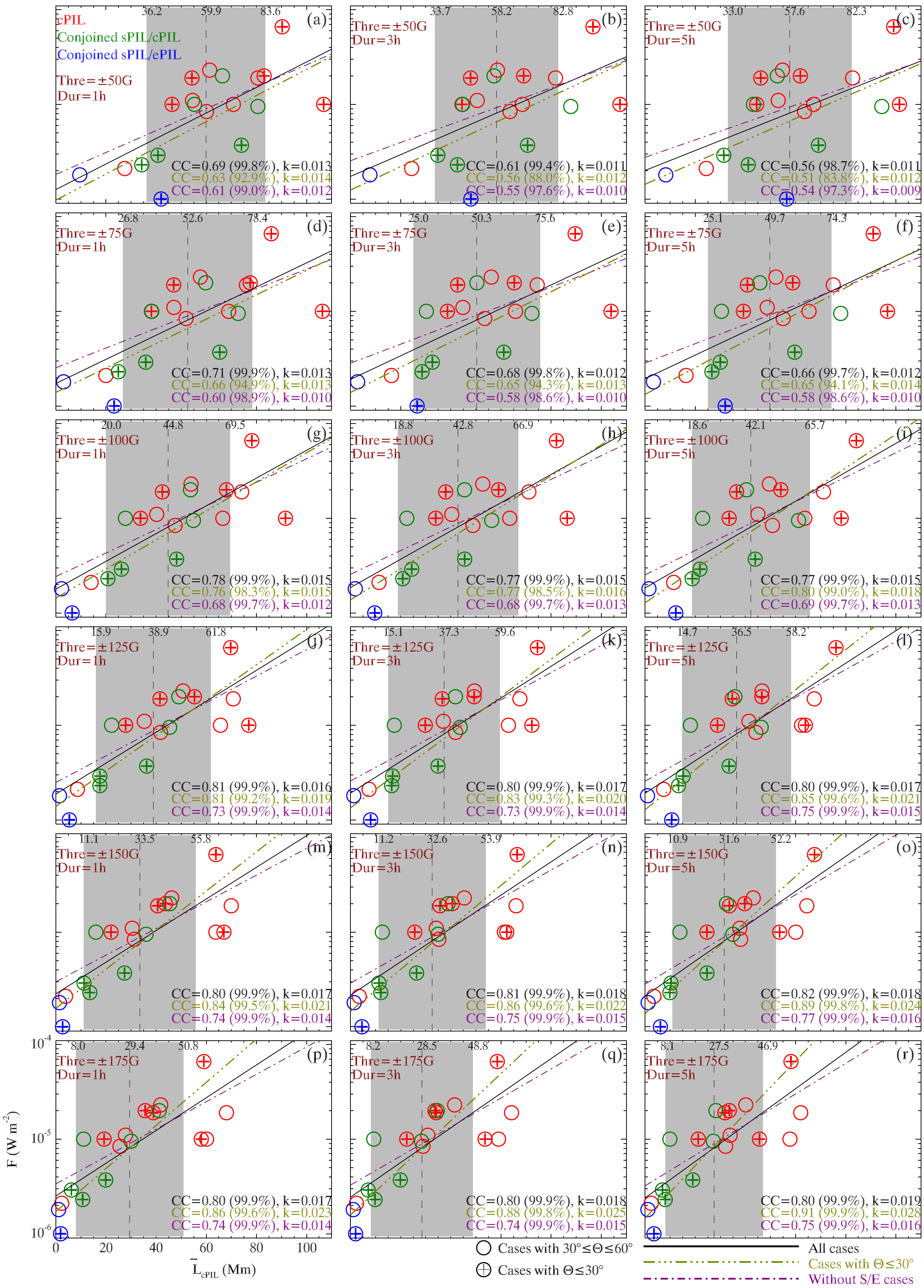

Figure 18. Scatter plots of the mean length of the collisional part of the PIL ($\overline{L}_{\mathrm{cPIL}}$) obtained from the B_{los} data set vs. the GOES 1–8 Å flux (F) for various thresholds and averaging durations. The layout is similar to Figure 17.

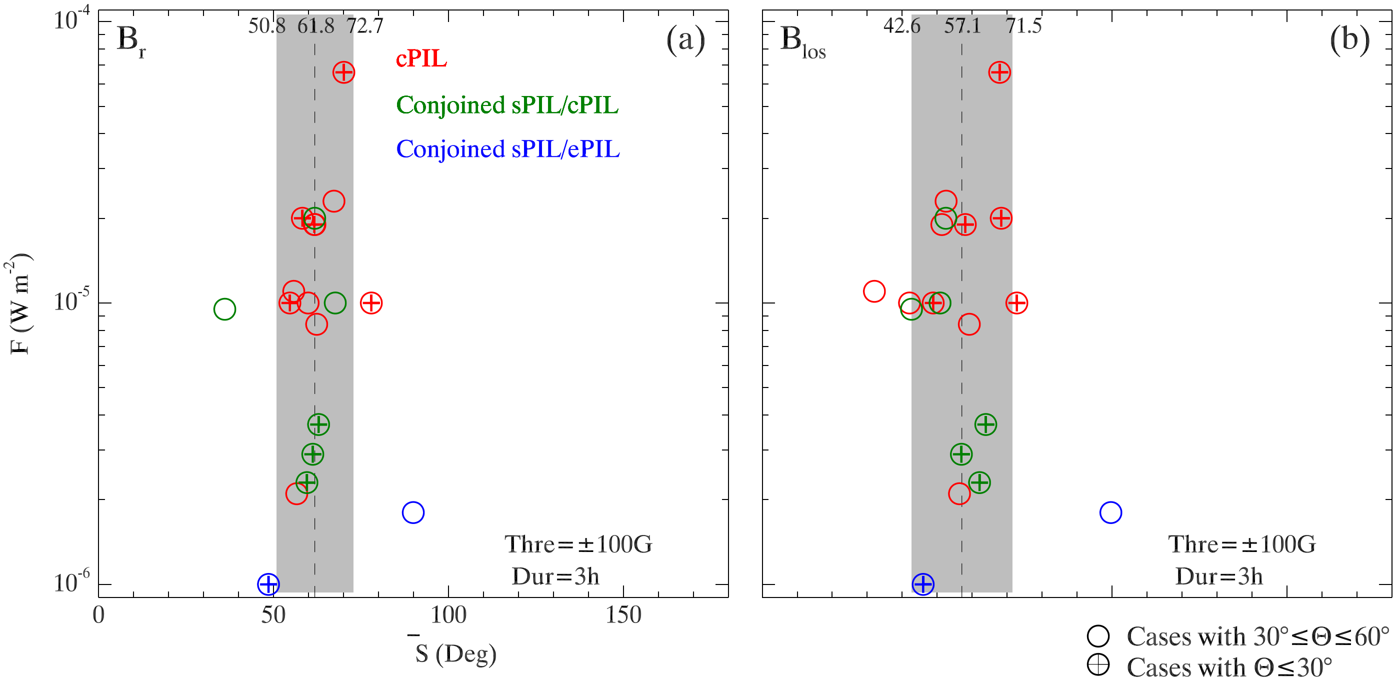

Figure 19. Scatter plots of the mean shear angle ($\bar{S}$) vs. the GOES 1–8 Å flux. $\bar{S}$ of each AR is averaged over three hours prior to the first major activity based on the collisional PIL part detected at the threshold of 100 G on the B_r data set in panel (a), and at 100 G on the $B_{\rm los}$ data set in panel (b). The vertical lines, shaded regions, and labels have similar meanings to those in Figure 17.

interactions during the flux emergence play the important role in driving the major solar activities. Moreover, the length of the collisional PIL may be a promising indicator in forecasting the major solar activities.

We acknowledge the use of data from SDO, GOES, and SOHO. We thank our anonymous referee for his/her constructive report, which helped to improve the paper significantly. We thank Kutsenko A., Abramenko V., and Pevtsov A. for providing the list of the emerging ARs. L.L. is supported by NSFC (11803096), the Fundamental Research Funds for the Central Universities (19lgpy27) and the Open Project of CAS Key Laboratory of Geospace Environment. Y. W. is supported by NSFC (41574165, 41774178). Z.Z. is supported by the Open Project of CAS Key Laboratory of Geospace Environment. J.C. is supported by NSFC (41525015, 41774186).

ORCID iDs

Lijuan Liu https://orcid.org/0000-0001-6804-848X
Yuming Wang https://orcid.org/0000-0002-8887-3919
Zhenjun Zhou https://orcid.org/0000-0001-7276-3208
Jun Cui https://orcid.org/0000-0002-4721-8184

References

Alissandrakis, C. E. 1981, A&A, 100, 197
Antiochos, S. K., DeVore, C. R., & Klimchuk, J. a. 1999, ApJ, 510, 485
Bernasconi, P. N., Rust, D. M., Georgoulis, M. K., & Labonte, B. J. 2002, SoPh, 209, 119
Bobra, M. G., Sun, X., Hoeksema, J. T., et al. 2014, SoPh, 289, 3549
Centeno, R. 2012, ApJ, 759, 72
Chen, C., Wang, Y., Shen, C., et al. 2011, JGRA, 116, A12108
Cheng, X., Ding, M. D., Zhang, J., et al. 2014, ApJ, 789, 93
Cheng, X., Guo, Y., & Ding, M. 2017, ScChD, 60, 1383
Chintzoglou, G., Zhang, J., Cheung, M. C. M., & Kazachenko, M. 2019, ApJ, 871, 67
Falconer, D. A., Moore, R. L., & Gary, G. A. 2002, ApJ, 569, 1016
Falconer, D. A., Moore, R. L., & Gary, G. a. 2006, ApJ, 644, 1258
Falconer, D. a., Moore, R. L., & Gary, G. a. 2008, ApJ, 689, 1433
Fan, Y. 2001, ApJL, 554, L111
Fan, Y. 2009, ApJ, 697, 1529
Fan, Y., & Gibson, S. E. 2004, ApJ, 609, 1123
Georgoulis, M. K., & Rust, D. M. 2007, ApJL, 661, L109
Gopalswamy, N., Yashiro, S., Michalek, G., et al. 2009, EM&P, 104, 295
Green, L. M., Kliem, B., & Wallace, A. J. 2011, A&A, 526, A2
Hoeksema, J. T., Liu, Y., Hayashi, K., et al. 2014, SoPh, 289, 3483
Kliem, B., & Török, T. 2006, PhRvL, 96, 255002
Kutsenko, A. S., Abramenko, V. I., & Pevtsov, A. A. 2019, MNRAS, 484, 4393
Leka, K. D., & Barnes, G. 2007, ApJ, 656, 1173
Leka, K. D., Barnes, G., & Barnes., G. 2003, ApJ, 595, 1277
Lemen, J. R., Title, A. M., Akin, D. J., et al. 2012, SoPh, 275, 17
Liu, L., Cheng, X., Wang, Y., & Zhou, Z. 2019, ApJ, 884, 45
Liu, L., Wang, Y., Wang, J., et al. 2016, ApJ, 826, 119
Mackay, D. H., Gaizauskas, V., & Yeates, A. R. 2008, SoPh, 248, 51
Moore, R. L., Sterling, A. C., Hudson, H. S., & Lemen, J. R. 2001, ApJ, 552, 833
Olmedo, O., Zhang, J., Wechsler, H., Poland, A., & Borne, K. 2008, SoPh, 248, 485
Pesnell, W. D., Thompson, B. J., & Chamberlin, P. C. 2012, SoPh, 275, 3
Scherrer, P. H., Schou, J., Bush, R. I., et al. 2012, SoPh, 275, 207
Schmieder, B., Archontis, V., & Pariat, E. 2014, SSRv, 186, 227
Schrijver, C. J. 2007, ApJL, 655, L117
Schrijver, C. J. 2009, AdSpR, 43, 739
Shibata, K., Masuda, S., Shimojo, M., et al. 1995, ApJL, 451, L83
Strous, L. H., & Zwaan, C. 1999, ApJ, 527, 435
Török, T., Kliem, B., & Titov, V. S. 2004, A&A, 413, L27
van Ballegooijen, A. A., & Martens, P. C. H. 1989, ApJ, 343, 971
van Driel-Gesztelyi, L., & Green, L. M. 2015, LRSP, 12, 1
Yan, X. L., Xue, Z. K., Pan, G. M., et al. 2015, ApJS, 219, 17